Generation of ultrafast broadband MIR pulses utilizing a NOPA, and its potential applications

by

Samuel R. Turner

Advisor: Markus B. Raschke
Spring 2023

Commitee Members:
Prof. Markus B. Raschke - PHYS/JILA
Prof. Jun Ye - PHYS/JILA
Prof. Ralph Jimenez - CHEM/JILA

Abstract

Keywords: NOPA, DFG, IR s-SNOM, AFM, Ultrafast

Broadband light sources are a highly valuable tool for many experiments in the fields of physics and chemistry. In particular, being able to generate ultrafast broadband mid-infrared (MIR) pulses is critical for experiments studying molecular vibrations or interactions on the ultrafast timescale. For generating these pulses, utilizing a Noncollinear Optical Parametric Amplifier (NOPA) can provide some significant advantages over traditional light sources. First, this paper will compare a few different MIR light sources currently used for IR spectroscopy, and what their disadvantages are. Then, it will provide an explanation of a NOPA and discuss the advantages and disadvantages it has over traditional light sources. Finally, it will present some potential experiments that a NOPA could be used for, and discuss why a NOPA is an excellent choice for these types of experiments.

Introduction

Generation of ultrafast broadband MIR pulses is highly valuable in the fields of materials science, physics, and chemistry. In the MIR region (3.0-16.0 μm), many molecular vibrational modes are resonant. Studying these modes can provide fascinating insight into the way molecules interact, and there are many potentially exciting experiments to be explored. There are three research fields that are of particular interest, IR spectroscopy, light-matter coupling, and plasmonic enhancement. Each of these experiments require broadband light sources in the MIR range. [1–3]

For IR spectroscopy, a broadband pulse allows for identifying and characterizing multiple responses simultaneously. These types of experiments have applications in the characterization and classification of materials, as well as determining chemical and molecular structure [1, 4–7]. Light-matter coupling requires a broadband pulse to observe peak splitting around a molecular transition. For these experiments, a broadband light source is critical to observe the entirety of the peak splitting, which can be quite large ($>$ 300 cm^{-1}). Potential applications for light-matter coupling research include coherent control, controlling chemical reactions, and photochemistry [2, 8]. Finally, plasmonic enhancement experiments study nanostructures that have a broad resonance, again requiring a broadband MIR light source. These research on these nanostructures could be applied to the development of high sensitivity chemical and biological sensors [3, 9]. A few examples of all three types of experiments can be seen in figure 1.

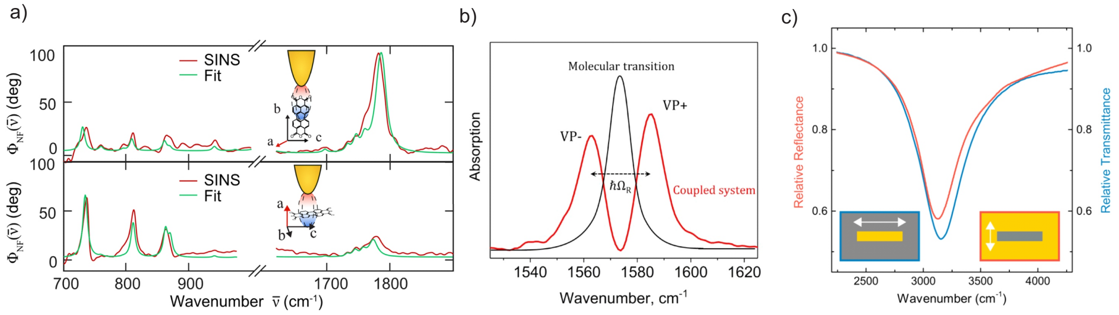

Figure 1: **a)** IR s-SNOM performed on PTCDA using a synchrotron light source. Using the high bandwidth of a synchrotron allows for each peak to be measured and characterized simultaneously. Figure from Ref [1]. **b)** An example of a spectrum measured in a vibrational strong coupling experiment. As the coupling strength between the molecules and the light increases, the splitting between the peaks will increase, requiring a broad pulse to measure it. Figure from Ref [2]. **c)** Spectra from a far-field measurement on a nanoslit array and a nano-antenna array. The response is quite broad, and to measure these structures in the near-field would require a light source with a very high bandwidth. Figure from Ref [3].

Currently these experiments are performed with a variety of traditional light sources that each have their own advantages and disadvantages. Synchrotrons have a very high bandwidth, but they are expensive to build and maintain, and require coordination to be effective [1, 5]. They also cannot generate ultrafast pulses, which can restrict the amount of potential experiments that they can be used for. Many molecular interactions occur on the femtosecond (fs) timescale, requiring an ultrafast pulse. On the other hand, Optical Parametric Amplifiers (OPA) and Optical Parametric Oscillators (OPO) can provide the ultrafast pulse necessary for those experiments, but they often restricted by their bandwidth [10–13].

There is a strong need for a highly available ultrafast broadband MIR light source. A Noncollinear Optical Parametric Amplifier (NOPA) and Difference Frequency Generation (DFG) setup can provide an effective method to generate the necessary pulses, and are much more accessible than a synchrotron. Compared to many traditional light sources, a NOPA/DFG setup has some potential advantages. A NOPA/DFG setup is capable of generating pulses greater than $>$ 400 cm^{-1}, that are also ultrafast. The setup is also highly tunable, being able to cover a substantial portion of the MIR range, and can be adjusted to cover the region of interest [14]. A comparison of these light sources and a few others can be seen in table 1.

MIR Light Sources

Light source	Typical bandwidth	Range	Pulse duration	Repetition rate	Reference
QCLs	CW	3.0-5.0 μm	ns	kHz - MHz	[15]
Lead-salt diodes	CW	3.3-4.2 μm	ns	kHz	[16]
OPA/DFG (Yb pumped)*	250 cm^{-1}	1.0 - 10 μm	5-200 fs	1 kHz - 10 MHz	[17]
OPO/DFG*	200 cm^{-1}	2.0 - 10.0 μm	200 fs	80 MHz	[11]
OPCPA*	200 cm^{-1}	2.0 - 5.0 μm	50-100 fs	1-100 kHz	[12, 13]
Supercontinuum	500 cm^{-1}	3-5.5 μm	150 fs	100 MHz	[18]
ALS (Synchrotron)	>3000 cm^{-1}	Unconstrained	60 ps	500 MHz	[5]
NOPA/DFG (Chen, et al.)	>400 cm^{-1}	5 - 11 μm	32 fs	50 kHz	[14]

Table 1: Comparison of MIR light sources. The values in this table are based on the references listed, and as such the details of each can be slightly different in practice. In particular, light sources marked with * are highly dependent on choice of crystal and pump laser, for more information see Ref [10, 17]

This paper will discuss the methods of NOPA/DFG, and present a few experiments that the setup can be used for. The first chapter will discuss IR s-SNOM and provide a full description of the setup. It will also present the methods that NOPA/DFG utilize to generate ultrafast broadband MIR pulses. The second chapter will show a characterization of the NOPA/DFG setup, and compare the measured parameters with the literature. The third chapter presents an IR s-SNOM experiment performed using a NOPA/DFG and discusses the results of the experiment. Finally, the fourth chapter discusses Vibrational Strong Coupling in Fabry-Perot cavities, and presents the results of the experiments performed using the NOPA/DFG to characterize the cavities.

Chapter 1

Broadband IR s-SNOM setup

In materials science, there are several ways of characterizing and imaging a material. One of the primary ways that these materials are studied is known as infrared scattering-type Scanning Near-field Optical Microscopy or IR s-SNOM. IR s-SNOM is performed by shining a laser onto an Atomic Force Microscopy (AFM) tip and measuring the light that scatters off the tip [1, 4, 6, 7]. The experiments performed for this thesis were IR s-SNOM experiments on a variety of materials using broadband mid infrared (MIR) pulses. The primary focus of this paper is to discuss these experiments and explore the advantages and disadvantages of using a broadband pulse.

This chapter will provide background information about the experiments performed. It will primarily focus on the foundational physics that describe the experiment and results. The first section will focus on IR s-SNOM and atomic force microscopy (AFM), and how they can be used as a method for characterizing a sample. The second section will discuss broadband pulse generation, and will contain several subsections. The first subsection is about the primary focus of the paper, a Noncolinear Optical Parametric Amplifier (NOPA). A NOPA allows for generation of broadband pulses that have significant advantages for s-SNOM over a more narrowband pulse. The next three subsections will discuss supercontinuum generation, second harmonic generation, and difference frequency generation respectively. Each of these three subsections discuss specific aspects of broadband pulse generation. By taking advantage of these nonlinear processes, broadband MIR pulses can be generated and used in IR s-SNOM experiments.

1.1 IR s-SNOM and Atomic Force Microsocpy

Atomic Force Microscopy

Atomic Force Microscopy (AFM) is a microscopy technique used for imaging the topography of a sample at the nanometer scale. The primary components of an AFM are the cantilever and a nanometer scale AFM tip; the setup can be seen in figure 1.1. When the tip is placed near a sample, the cantilever will bend due to the attractive or repulsive forces acting on the tip [19, 20]. As the cantilever bends, a laser reflected off the cantilever is detected by a four quadrant photodetector. The small changes in voltage difference measured by the detector are used to precisely measure the motion of the cantilever. By detecting the motion of the cantilever, which corresponds to the forces acting on the tip, an AFM is able to detect small variations in the topography of the sample [19, 20].

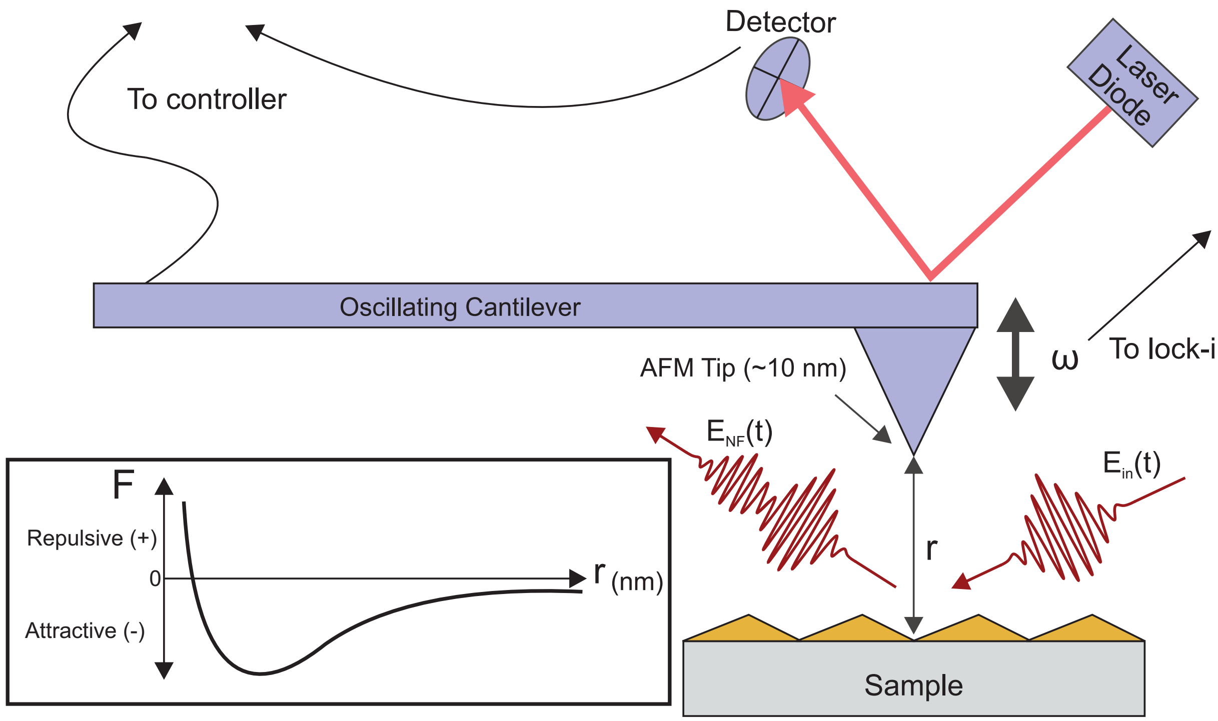

Figure 1.1: AFM schematic showing the oscillating cantilever with a driving frequency ω. The force measured by the detector is used as the imaging signal. The driving (tip tapping) frequency can be used to modulate and demodulate the incoming laser pulse $\mathrm{E_{in}(t)}$, and will be discussed further in the next section. **Inset:** Force curve showing the force F acting on the tip relative to the position from the sample r.

The force F acting on the tip can be calculated using the potential the following equation [20]:

$$F = -\frac{\partial V}{\partial r} \tag{1.1}$$

There are two primary modes that an AFM can image a sample. The first is known as contact mode, where the cantilever is held at a constant position and the height between the sample and the tip is measured directly [19]. Unfortunately, using an AFM in contact mode causes a strong lateral (shear) force on the sample when the tip scans across it, and can easily damage the sample. Instead, oscillating the cantilever with a driving frequency ω restricts the amount of time that the tip can be in contact with the sample, therefore reducing the potentially damaging lateral force. Oscillating the cantilever in this way is known as tapping mode [19]. When in tapping mode, a target voltage setpoint can be chosen. With each oscillation (or bending) the voltage difference on the detector changes, and a correcting voltage is applied to the sample stage in order to restore the voltage to the setpoint [20]. The height difference that the sample stage needs to move to restore the voltage difference is the height of the sample.

To get a full image of the topography of a sample, the tip is scanned across the surface in a pattern known as a raster scan. At each point, the height is recorded and displayed in an AFM image [19, 20]. While these images are primarily used to determine the topography of a sample, the tapping amplitude and phase can be detected and imaged as well. Sample AFM images can be seen in figure 1.2.

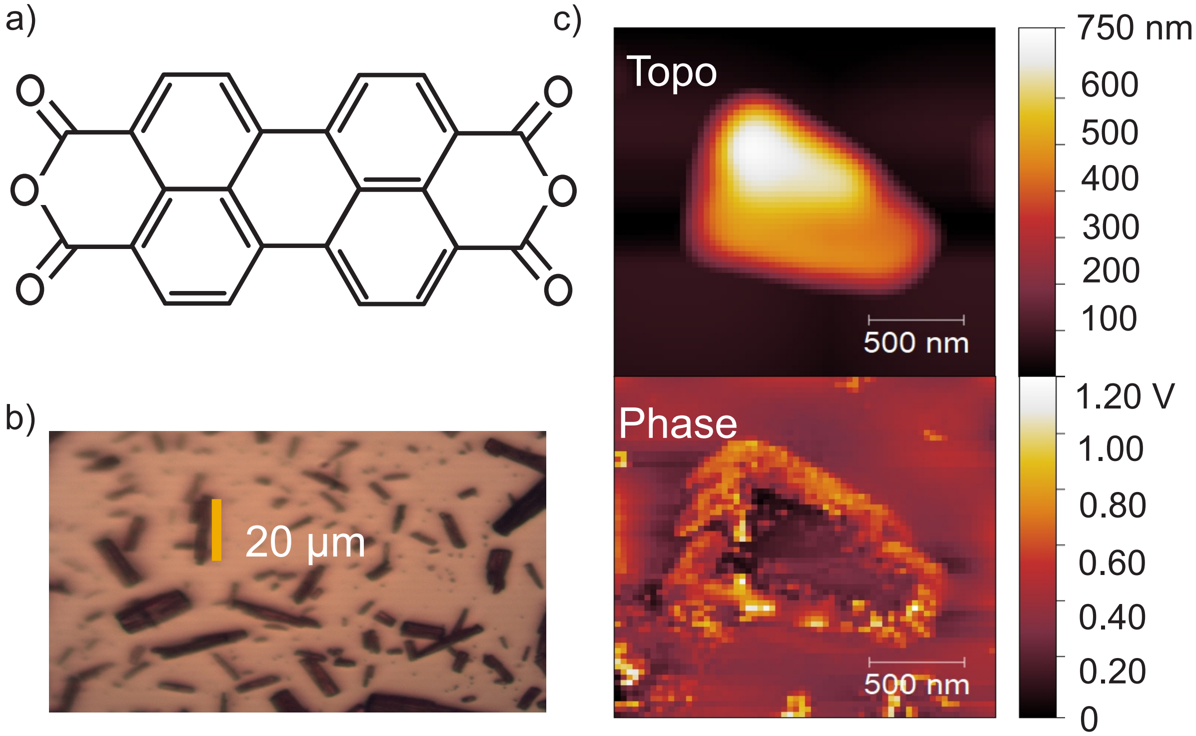

Figure 1.2: **a)** Molecular structure of Perylenetetracarboxylic dianhydride (PTCDA). **b)** Optical microscope image of the PTCDA sample. The image shows a multitude of different microcrystals, varying significantly in size and shape. **c)** AFM image of a PTCDA microcrystal showing the topography (TOPO) and tapping phase (Phase) information.

IR s-SNOM

Infrared scattering-type Scanning Near-field Optical Microscopy (IR s-SNOM) is a spectroscopy technique used to study the optical response of different materials. In the IR range, these optical responses are caused when the atoms inside a molecule move relative to each other. These vibrational modes are resonant in the mid infrared (MIR) range (3-12 μm), and can provide insight about the characteristics and properties of a given material. Some of the interesting properties to study include chemical morphology and identity, molecular orientation, and intermolecular coupling. IR s-SNOM provides a method to characterize these responses with a nanometer scale resolution [1,7].

To perform IR s-SNOM, IR (or MIR) light is sent into a Michelson Interferometer (see figure 1.3). When it enters the interferometer, the light is split into two beams, one that will go to the sample, and one that is used as a reference. The sample beam is directed onto the sample where it scatters off the AFM tip. The scattered light is collected and focused by a parabolic mirror that directs it back toward the beam splitter. At the same time, the reference beam is directed through a reference arm where it is reflected back to the beam splitter as well. The reference arm is placed on a movable stage so that the time delay between the pulses can be adjusted. From the beam splitter, the two beams are overlapped onto a Mercury-Cadmium-Telluride (MCT) detector which detects the MIR signal [4,6,7].

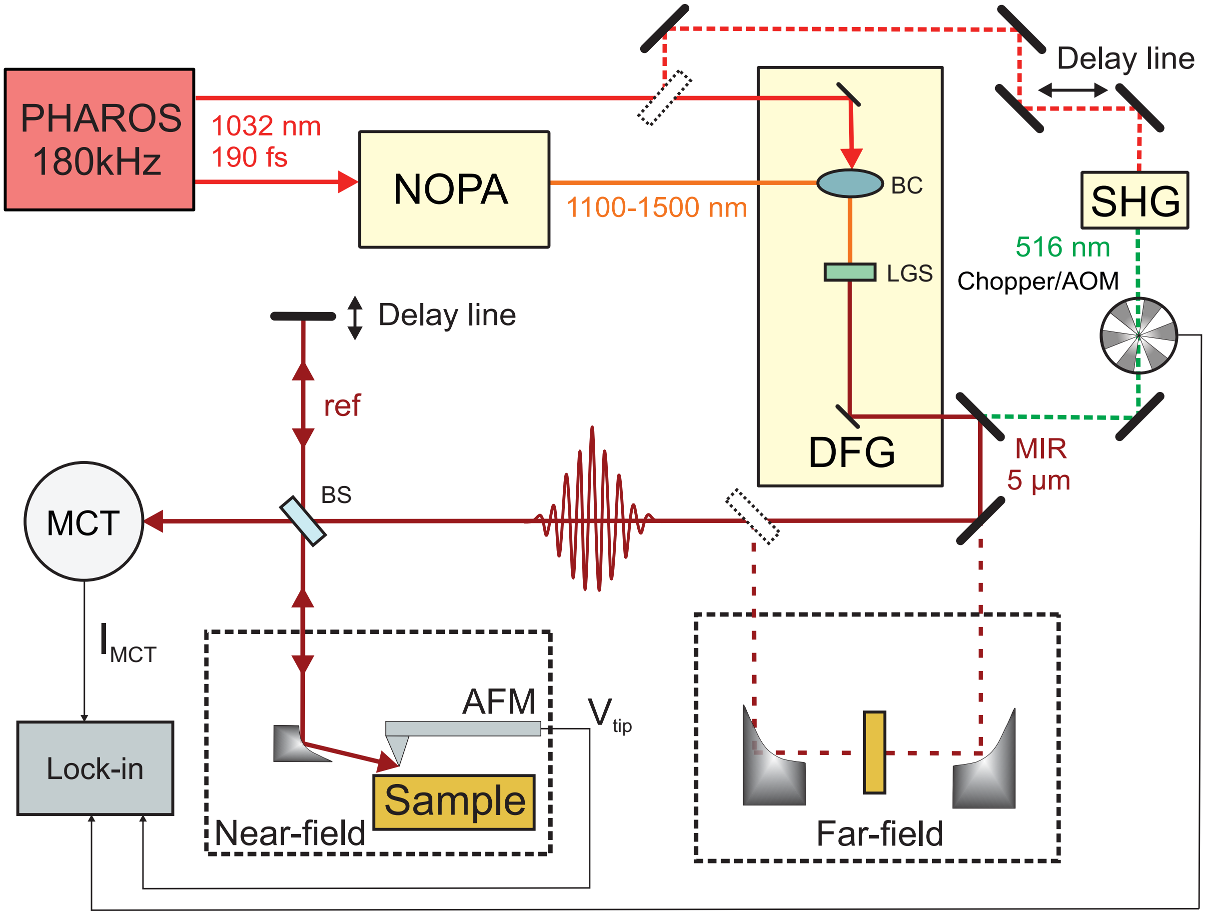

Figure 1.3: IR s-SNOM setup using an interferometer. A PHAROS laser (Light Conversion, 190 fs, 180 kHz, 1032 nm) is used to generate broad pulses spanning the visible and near-infrared (NIR) regions with a Noncollinear Optical Parametric Amplifier (NOPA). The pulse in the NIR is used to generate an MIR pulse using difference frequency generation (DFG). Then, the MIR pulse is split into sample and reference beams. After the sample beam interacts with the sample, it is overlapped with the reference beam onto an Mercury-Cadmium-Telluride (MCT) detector. The signal is modulated by the tip tapping frequency ω when it interacts with the sample, and the signal is then demodulated in the lock-in. Varying the time delay between the two pulses generates an interferogram which can be transformed to the frequency domain from the time domain by Fourier transform, showing the signal as a spectrum. Additionally, the setup can be configured to perform pump-probe (dashed 1032 nm beam path) and far-field measurements as well. Far-field measurements will be discussed in a later section, and for a description of pump probe measurements see [21]. **Key:** BC- Beam Combiner, SHG - Second Harmonic Generation, BS - Beam splitter

The detected signal on the detector will be a combination of the three electric field components that make up the beam [4, 6, 7]. $\widetilde{E}_{ref}$ is the reference electric field from the reference arm. $\widetilde{E}_{NF}(\omega)$ is the near field component which is scattered from the tip, and is dependent on the tip tapping frequency ω. Finally, $\widetilde{E}_{FF}$ is the background far-field component. The intensity on the detector can be given by [6]:

$$I_{MCT} = \widetilde{E}_{ref}^2 + \widetilde{E}_{NF}(\omega)^2 + \widetilde{E}_{FF}^2 + 2\widetilde{E}_{ref}\widetilde{E}_{NF}(\omega) + 2\widetilde{E}_{ref}\widetilde{E}_{FF} + 2\widetilde{E}_{NF}(\omega)\widetilde{E}_{FF} \tag{1.2}$$

This signal is noisy, and the near field signal $\widetilde{E}_{NF}(\omega)$ is far too small to see any changes. In order to minimize the background, the signal is demodulated at the tip tapping frequency ω using a Lock-in Amplifier. After demodulation, the intensity only contains components that depend on ω and becomes much simpler [6]:

$$I_{MCT} = \widetilde{E}_{NF}(\omega)^2 + 2\widetilde{E}_{NF}(\omega)\widetilde{E}_{FF} + 2\widetilde{E}_{ref}\widetilde{E}_{NF}(\omega) \tag{1.3}$$

$\widetilde{E}_{NF}(\omega)$ is quite small, and as a result, $\widetilde{E}_{NF}(\omega)^2$ can be ignored. This leaves two remaining terms. The $2\widetilde{E}_{NF}(\omega)\widetilde{E}_{FF}$ is known as the self-homodyne term. There is still significant background from the $\widetilde{E}_{FF}$ term, but by demodulating at different harmonics of the tip tapping frequency $n\omega$, the far-field data can be suppressed. At higher harmonics of ω, the far-field is suppressed, but the signal becomes smaller as well. For the IR s-SNOM experiment in this paper, the data was demodulated at 2ω, which is known as the second-harmonic. The final term $2\widetilde{E}_{ref}\widetilde{E}_{NF}(\omega)$ is known as the heterodyne term, which is dependent on the optical path difference between the two beams. The heterodyne term amplifies the near-field signal enough that it can be detected in a process known as heterodyne amplification [6].

However, the near-field data from the lock-in does not show the entire response of the material. To see the full optical response, an interferogram needs to be generated by adjusting the optical path difference between the signal and reference arms. By changing the length of the reference arm, a phase change is introduced between the two beams (changing the heterodyne term), which dramatically changes the signal detected by the MCT. The change in signal results in an interference pattern (interferogram) in the time domain that can be changed into the frequency domain by Fourier transform. The frequency domain data will have both real and imaginary components which can be plotted as spectra. The real part shows the dispersion of the material and is represented as the Fourier transform amplitude. The imaginary part is the spectrum of the material and can be seen in the Fourier transform phase [6].

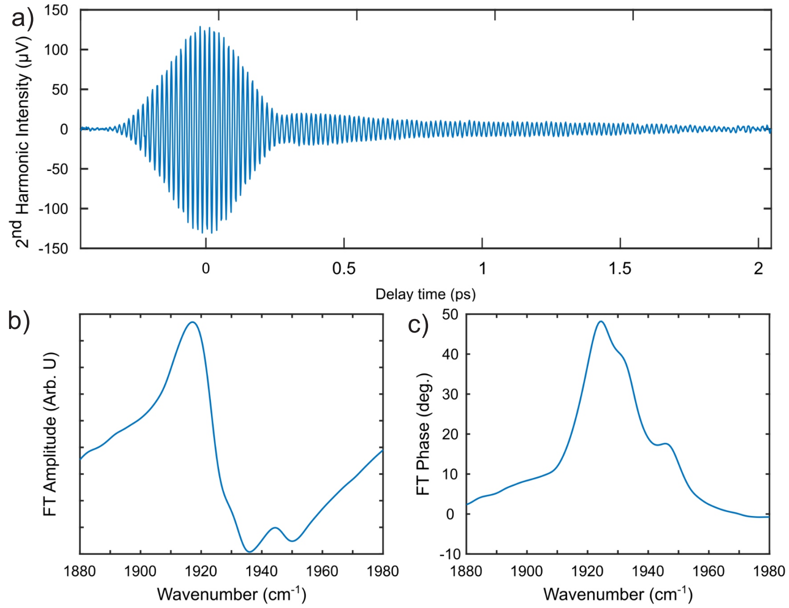

Figure 1.4: Sample interferogram and near field data taken on RuOEP nanocrystals. **a)** Inteferogram generated by varying the optical path difference between the beams. The signal is the voltage (intensity) of the second harmonic signal measured on the sample. **b)** Amplitude component of the spectrum after Fourier transform. **c)** Phase component of the spectrum after Fourier transform. From Ref [6]

Alternatively, a specific fixed reference arm position can be chosen. Generally, this point is chosen to be the maximum value of the interferogram. At this mirror position, an AFM scan is taken, giving the signal responses at different positions. Next, the mirror is moved to a second position at a distance determined by the wavelength $\lambda/4$, and another AFM scan is taken. Using these two scans is known as 2-phase heterodyne detection, which gives the signal amplitude without the background noise from the self-homodyne term. 2-phase heterodyne detection is useful for imaging a sample as well, allowing responses on a sample to be localized and visualized.

1.2 Broadband MIR pulse Generation

Noncolinear Optical Parametric Amplifiers

Generation of ultrafast broadband MIR pulses is challenging. Many traditional light sources (QCLs [15, 22–24], lead-salt diodes [16, 25], and fiber lasers [10, 26] among others [5, 11–13, 27–30]) can either generate a broadband pulse but lack tunability, or they have a broad tunability but lack the ability to generate broad pulses. A Non-collinear Optical Parametric Amplifier (NOPA) can provide high tunability as well as a broad pulse. The primary purpose of a NOPA is to generate broadband visible and NIR pulses that can then be converted into MIR pulses (and amplified) using Difference Frequency Generation (DFG). By combining the NIR pulse from the NOPA with the 1032 nm pulse from the PHAROS, an MIR pulse can be generated that is both ultrafast and broadband. A NOPA-DFG setup is capable of generating pulses with a Full Width at Half Maximum (FWHM) of 400 cm^{-1} (can be significantly broader in principle), with a wide tunability of $>$2000 cm^{-1} [14, 31].

There are two main advantages of using a NOPA. Primarily, a NOPA can generate a broad pulse that can be used to study broad optical responses, as well as being able to observe several vibrational modes simultaneously. The second main advantage is that a NOPA provides a high level of tunability, which allows the setup to perform a variety of experiments in quick succession, as well as targeting a wide range of modes with minimal adjustments. [14, 31, 32]. The setup of the NOPA can be seen in figure 1.5.

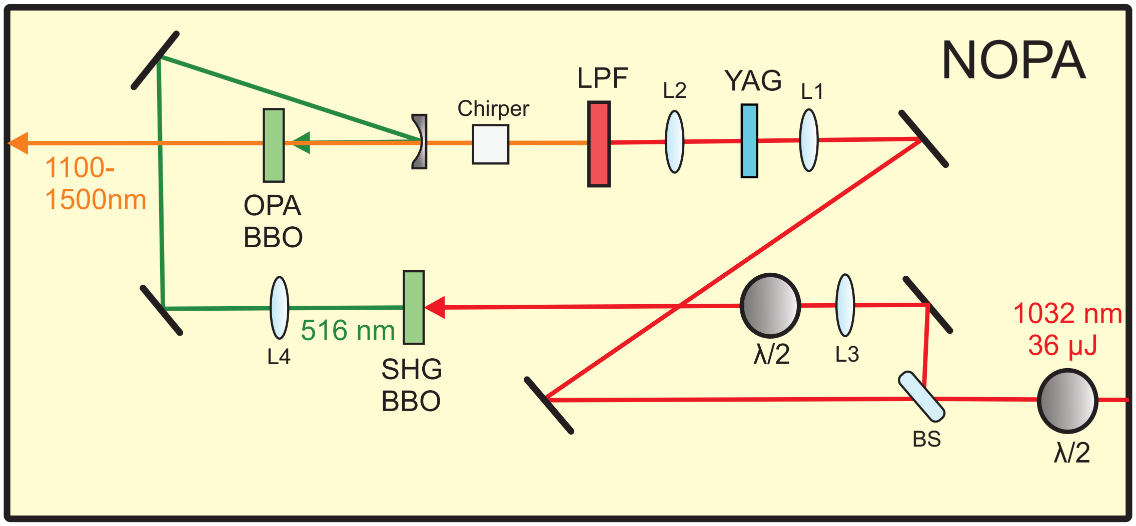

Figure 1.5: Optical Layout of the NOPA. A 1032nm pulse (red) enters from the bottom right. Using a half-wave plate ($\lambda/2$), the pulse is polarized and then split into two beams. By adjusting the polarizaion, the amount of power going to each beam can be adjusted. One beam is used to generate white light in the Yttrium Aluminum Garnet (YAG) crystal, while the other undergoes second harmonic generation (SHG) inside a Barium Borate (BBO) crystal (SHG BBO) to become a 516 nm green pulse. The white light generated passes through a long pass filter (LPF) to remove the visible part of the spectrum, and it then passes through an optional chirper block to chirp the pulse (increases pulse width). The two pulses are then recombined in another BBO crystal (OPA BBO) where the desired amplification occurs. The pulse that exits the NOPA (orange) is 1100-1500 nm tunable, with a bandwidth of approximately 100 nm. **Key:** L1-L4 - lenses; BS - Beamsplitter.

Supercontinuum generation

The 1032 nm pulse from the PHAROS enters the NOPA and is split into two beams. The first beam is focused onto a Yttrium Aluminum Garnet (YAG) crystal, where a supercontinuum is generated. Supercontinuum generation is a process involves several different nonlinear processes, but all of these processes are highly reliant on the Kerr Effect. The Kerr Effect is a nonlinear optical process that causes the refractive index of a material to change in response to an applied electric field [33]. The change in refractive index $n(I)$ can be described as a function of the linear refractive index n_0, the nonlinear refractive index n_2, and the intensity of the applied field I [34]:

$$n(I) = n_0 + n_2 I + ... \tag{1.4}$$

Most importantly, this equation shows that the refractive index of the material is dependent on the intensity of the laser pulse. Due to the multi-directional wavefronts of the beam, as the intensity increases, the refractive index increases, causing the wavefronts of the pulse to converge toward the center of the crystal. The wavefronts converging in this way is known as self-focusing, and this effect is critical to supercontinuum generation.

Self-focusing further focuses the beam inside the crystal, and as the focus continues to get smaller, the beam begins to excite bound electrons in the crystal, creating a filament. A filament is a channel of high energy plasma that emits coherent white light [34]. A wave is coherent if they have an identical frequency and waveform. Coherent light is particularly important for this application because it allows for the generation of the interferograms necessary in s-SNOM. If intensity of the original pulse is too high, multiple filaments can be generated in succession, as the high intensity white light is refocused creating another filament. This successive filamentation is primarily caused by divergence created by the plasma. The creation of multiple filaments causes the light to be much less stable, so the incident pulse must be carefully adjusted to find the minimum intensity required for supercontinuum generation (while maintaining the focus on the crystal).

The newly generated white light is already broad, but it is made significantly broader by another nonlinear optical effect known as self-phase modulation. Self-phase modulation causes the pulse to be broadened symmetrically around the center frequency. As the white light passes through the crystal, the Kerr effect causes the phase shift of the pulse to change as a function of time [34]. The changing phase introduces a chirp into the incident pulse, which changes its instantaneous frequency. The time dependent chirp creates new frequencies as the pulse passes through the length of the crystal, which has the desired effect of broadening the spectrum [34, 35]. The light generated by the filament is coherent and high energy, and it is broadened symmetrically by self-phase modulation. These processess have the desired effect of creating a coherent broad pulse that can be amplified. A sample supercontinuum from [34] can be seen in figure 1.6

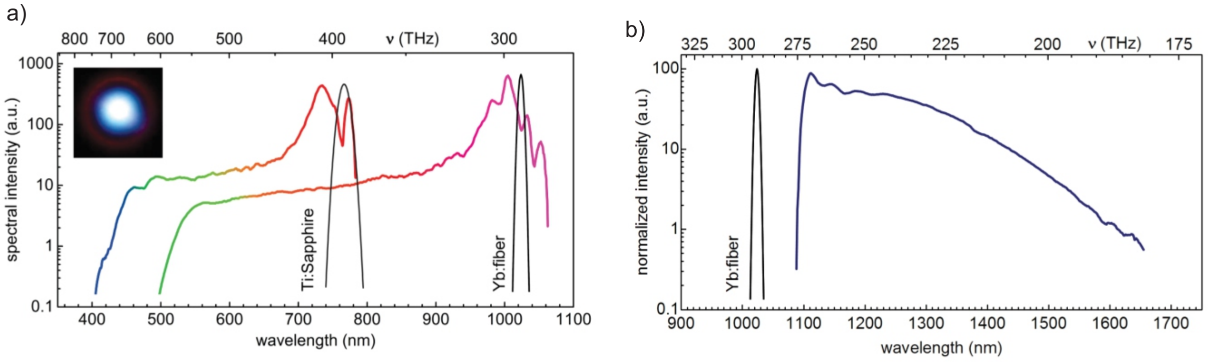

Figure 1.6: Generated spectra using a 4mm YAG crystal with two different lasers (Ti:Sapphire and Yb:Fiber). Yttrium Aluminum Garnet (YAG) is chosen due to its high optical damage threshold. **a)** White light spectrum (inset: Beam profile). **b)** Near-infrared (NIR) spectrum. From Ref [34]

Second Harmonic Generation

Pulse amplification requires two incident pulses. The pulse to be amplified is known as the seed pulse. In this case, the seed pulse is the supercontinuum generated by the YAG crystal. The second pulse is known as a pump pulse, which in this case is a visible 516 nm pulse. The PHAROS laser generates a 1032 nm pulse, which needs to be converted into the visible pump pulse, which is done by second harmonic generation (SHG). SHG (also known as frequency doubling), is a nonlinear optical process which depends on the polarization density (or the electric dipole moment per unit volume) $P(t)$. The polarization density changes depending on the applied electric field $E(t)$, and the n-th order susceptibilities of the optical medium χ^n. $P(t)$ can be written as [36]:

$$P(t) = \epsilon_0 \left(\chi^1 E(t) + \chi^2 E^2(t) + \chi^3 E^3(t) + ...\right) \tag{1.5}$$

The most important consequence of this equation is that the polarization density changes depending on the nonlinear susceptibilities of the material. A material that has a strong second order response χ^2 will have a much higher polarization density than a material that only has a strong first order response χ^1. In nonlinear materials, the second order responses are higher, and as a result the polarization density of the material is higher. A higher polarization density in these materials causes incident light to behave in unique ways, one of which is SHG.

SHG causes two beams of light with the same frequency to interact and generate a new beam with twice the energy of the initial beam (which corresponds to doubling the frequency). The frequency doubling occurs as a result of the increased polarization density in the material. SHG is a special case of another nonlinear optical process known as sum frequency generation (SFG), which occurs when two incident beams interact inside a medium to generate a third beam. SFG occurs in all nonlinear materials, but the efficiency of the process is highly dependent on the phase matching of the two input pulses. Phase matching occurs when a specific phase relationship between the beams is reached and maintained. For SFG (and SHG), the phases must be matched such that the waves interfere constructively. As such, the equation for the phase matching Δk depends on the wavevectors of each incident beam k_1, k_2 and the resulting beam k_3 [36]:

$$\Delta k = k_1 + k_2 - k_3 := 0 \tag{1.6}$$

If the beams are perfectly phase matched, $\Delta k = 0$ and $k_1 + k_2 = k_3$. Perfect phase matching requires that the group velocity of the wavevectors to be the same. Unfortunately, this is not possible in many materials due to dispersive effects caused by a frequency dependent refractive index. To solve this problem, birefringent crystals provide a material with a polarization dependent refractive index. By adjusting the orientation of the crystal, the refractive indexes can be matched, which causes the group velocity to be matched as well. As the beams approach perfect phase matching, wave-mixing occurs, and they generate a new beam with frequency ω_3 that depends on the frequency of the incident beams, ω_1 and ω_2 [36]:

$$\omega_3 = \omega_1 + \omega_2 \tag{1.7}$$

The resulting beam has a frequency which is the sum of the frequencies of the incident beams, which can be visually represented in figure 1.7.

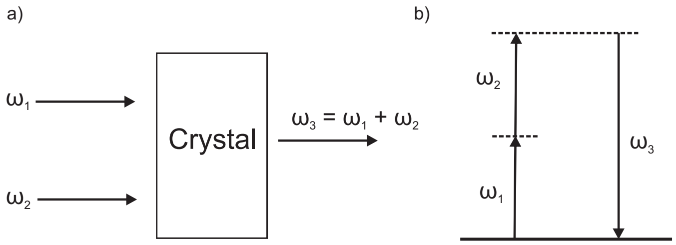

Figure 1.7: Visual representation of SFG. **a)** Image showing the summing of the frequencies ω_1 and ω_2 to generate ω_3. The efficiency of the conversion is highly dependent on the phase matching between the pulses. Adjusting the angle of the crystal will change the phase matching angle and is used to optimize the output pulse. **b)** State representation of SFG, where ω_1 and ω_2 are summed and create a virtual state which then emits ω_3.

Similarly, second harmonic generation sums the frequencies, but the frequencies of the incident beams are the same (i.e. $\omega_1 = \omega_2$). Substituting into the previous equation, it follows:

$$\omega_3 = \omega_1 + \omega_1 = 2\omega_1 \tag{1.8}$$

The newly generated pulse will have a frequency of twice that of the incident pulse (half the wavelength). Given the 1032 nm output pulse from the PHAROS, the new wavelength will be approximately 516 nm. The generated pulse will not be monochromatic, which allows for greater amplification of the supercontinuum. Once generated, the pump pulse can be used to amplify the previously generated supercontinuum in the target wavelengths. Using the 516 nm pulse instead of the 1032 nm pulse from the PHAROS allows for better phase matching. If 1032 nm were used, the amplification would be much less efficient.

The amplification occurs due to a process known as Optical Parametric Amplification (OPA), which can be represented visually in figure 1.8. In a nonlinear crystal (BBO in this case), the high intensity (high frequency) pump beam amplifies the lower intensity (lower frequency) seed to generate a signal beam, as well as a third beam known as the idler [17]. The idler must be generated so that energy conservation is not violated, but for these experiments the idler is not used.

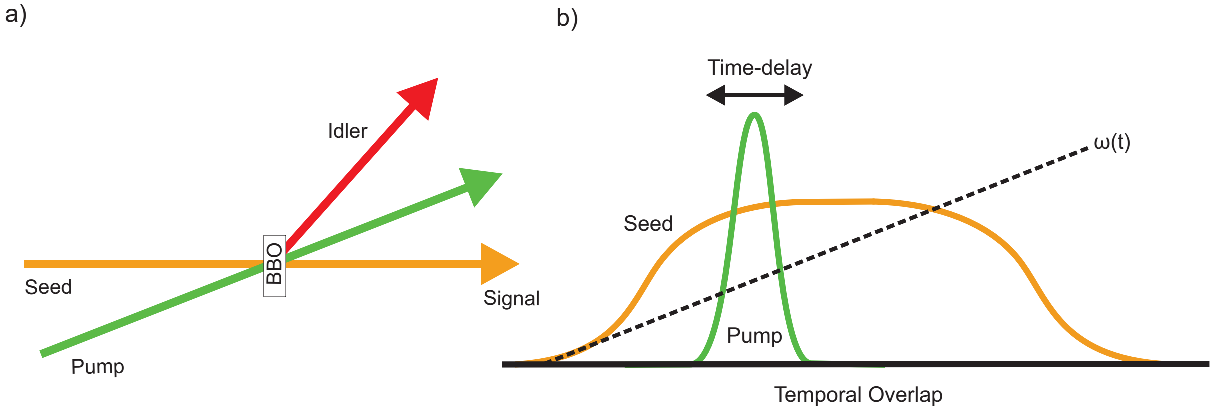

Figure 1.8: **a)** Visual representation of OPA in a BBO crystal. The low frequency seed pulse is amplified by the high frequency pump pulse to generate the signal pulse as well as an idler pulse. **b)** Visual representation of the overlap between the seed and pump pulses. Adjusting the time delay changes the temporal overlap between the pulses, which modifies which wavelengths are amplified. This provides the NOPA with a high level of tunability.

OPA is responsible for some of the significant advantages of the NOPA/DFG setup. By adjusting the temporal of the seed and pump, selected portions of the supercontinuum can be amplified, which gives the NOPA its wide range of tunable wavelengths. In a standard (collinear) OPA setup, the pulse's group velocities do not match, which causes pulse lengthening [34]. However, when using a NOPA, the noncollinear geometry allows generation of ultrashort (< 20 fs) pulses by avoiding this pulse lengthening. The noncollinear setup does have the consequence of causing the idler pulse to become spectrally dispersed, but this is not an issue for these experiments as the idler pulse is discarded. [34]

Difference Frequency Generation

In a similar fashion, Difference Frequency Generation (DFG) is another nonlinear optical process that occurs in nonlinear crystals. DFG usually occurs at an entirely different phase matching angle than SFG, which has the benefit of preventing SFG and DFG from occuring simultaneously. DFG occurs when a strong wave ω_3 and weak wave ω_1 enters the crystal. The wave interactions generate a new wave that is a difference of the frequencies of ω_3 and ω_1. A visual representation of DFG can be seen in figure 1.9. The generated wave will have a frequency ω_2 give by [36]:

$$\omega_2 = \omega_3 - \omega_1 \tag{1.9}$$

The new frequency is now a difference between the incident beams, instead of a sum of their frequencies. This process can also be interpreted as an amplification of ω_1, and results in the creation of an idler wave ω_2. However, unlike in the OPA occuring in the DFG, the idler wave is not discarded in this situation.

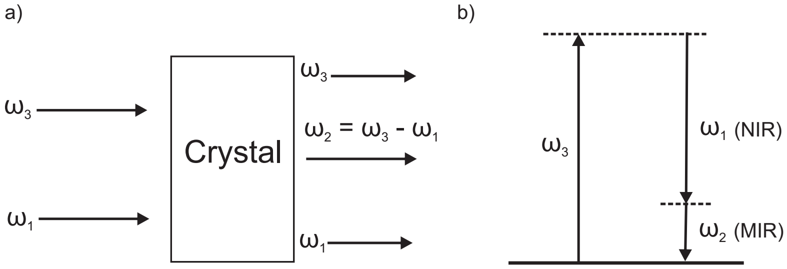

Figure 1.9: Visual representation of DFG.

For IR s-SNOM, DFG is primarily used to generate the MIR frequencies needed to excite materials. DFG allows generation of MIR frequencies that could not be normally be generated using traditional laser methods. In the next section, a sample calculation of the NOPA/DFG setup being used to generate MIR pulses will be shown.

Chapter 2

NOPA Characterization

The first experiment using this setup (seen in figure 1.3) was a full characterization of the NOPA. This was done to fully understand exactly what the NOPA/DFG setup is capable of, and to explore the potential advantages and disadvantages of the setup. It also provided a record of what potential spectra can be created by NOPA/DFG, allowing for future experiments to be more accessible. This chapter will discuss the methods and results of this characterization experiment.

2.1 Methods

Determining target wavelengths

Before the experiment could be performed, the target wavelength to tune the NOPA at in order to achieve a specific target wavenumber after DFG needed to be identified. The target wavelength for the NOPA λ_{target} [nm] can be calculated from the DFG value $\bar{\nu}$ [nm^{-1}] using the laser wavelength λ_{Pump} [nm] using the difference frequency generation equation:

$$\bar{\nu} = \frac{1}{\lambda_{Pump}} - \frac{1}{\lambda_{target}} \tag{2.1}$$

Solving for λ_{target} gives:

$$\lambda_{target} = \frac{1}{(1/\lambda_{Pump}) - (\bar{\nu})} \tag{2.2}$$

As an example calculation, using 1250 cm^{-1} as the target DFG output wavenumber $\bar{\nu}$, we receive a NOPA target wavelength of 1184 nm.

$$1184 \text{ nm} = \frac{1}{(1/1032 \text{ nm}) - (1250 \text{ cm}^{-1}/10^7)}$$

This equation can also be used to calculate a potential output spectrum from a given NOPA spectrum. For each wavelength of a NOPA output spectrum, the DFG output wavenumber can be calculated. When each calculated wavenumber is combined, the ideal DFG spectrum is obtained. These ideal DFG spectra will be discussed further in the next section. Using this equation, a center wavelength for the NOPA was calculated for each target DFG wavenumber. The chosen target DFG wavenumbers (in cm^{-1}) for the first round of measurements were $< 1100, 1100, 1150, 1200, 1250, 1300, 1350, > 1350$. At the edge of the range, the target DFG wavenumber was the minimum and maximum NOPA output that could be tuned.

NOPA tuning

In order to fully characterize the setup, two distinct measurements needed to be made at several different chosen target wavenumbers. First, the output spectra of the NOPA was measured before DFG using a rotating grating spectrometer (APE waveScan, 200 nm to 6 μm). As the spectrum was measured, the time-delay between the pump and seed pulses was adjusted, changing which frequencies are amplified in the crystal (see figure 1.8). Once the target center wavelength was reached, the NOPA output spectrum was optimized by adjusting the spatial overlap and the phase matching angle in the OPA BBO crystal. Once a sufficiently broad pulse was obtained (once it could not be made any broader without sacrificing a gaussian shape or significantly reduced power), the spectrum was saved to be used to calculate the ideal DFG spectrum.

In reality, the spectrum will not be ideal, and will suffer from non-uniform conversions in the DFG crystal (LiGaS, or LGS), absorptions from water in the air or optics, among other non-ideal effects. The expected conversion efficiency for an LGS crystal is approximately 60% [14]. For this experiment, the approximate calculated DFG spectrum is sufficient for the purpose of determining the target wavelength and bandwidth.

Calculating the ideal DFG spectrum was done by a Python script to determine if the spectrum was properly centered (and to compare with the spectrum measured by the interferometer in the future). The script read the NOPA spectrum file and processed the data into a usable format, and then converted each wavelength to its respective DFG output wavenumber. Then both spectra were plotted simultaneously. One pair of spectra can be seen in figure 2.1.

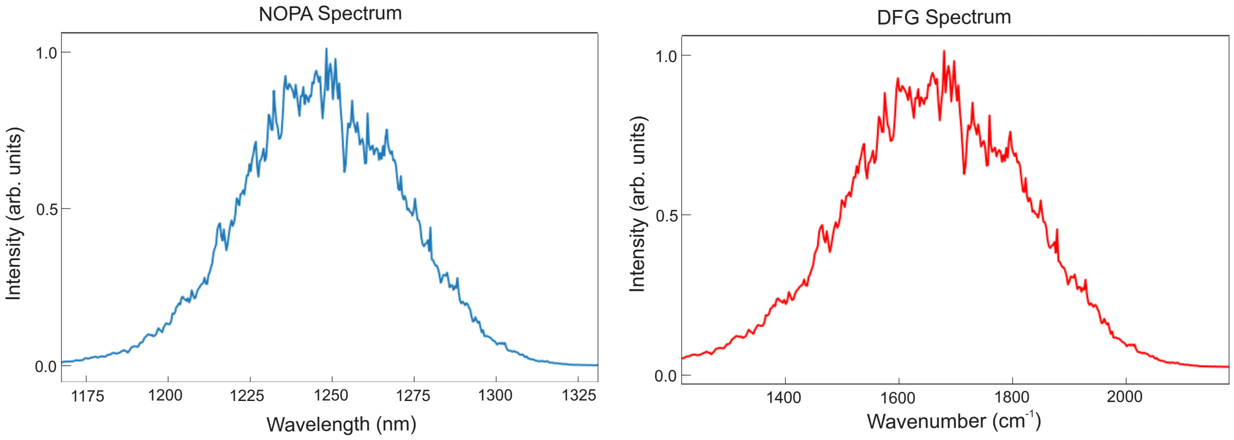

Figure 2.1: A pair of NOPA/DFG spectra calculated using a Python script. The calculation followed equation 3.1, where for a given input NOPA wavelength, the output DFG spectrum could be calculated. The target wavelength for this NOPA spectrum was 1249 nm.

Once it was determined that the spectrum was sufficient, the spectrometer was removed and the DFG output power was optimized. This was done in a similar way to that of the NOPA, where the temporal and spatial overlap, and the phase matching angle were optimized in a cycle until the maximum output power was obtained (2-5 mW). It is important to note that the DFG power was measured after an NIR filter, to remove any remaining NIR pump. After the filter, the goal of creating an ultrafast broadband MIR pulse has been accomplished.

The DFG spectra was measured using a Michelson interferometer. By placing a mirror in the beam path before the pulse reaches the AFM (see figure 1.3) perpendicular to the beam, the signal will only be the laser spectrum. The signal is measured in a similar fashion using an MCT detector, and an interferogram is generated. After Fourier transform, the laser spectrum can be seen. Comparing this spectrum to the spectrum that was calculated using the Python script can show any non-ideal absorptions. After the spectrum is collected, the experiment can easily be repeated by replacing the APE spectrometer and adjusting the NOPA center wavelength to the next target.

The NOPA was additionally characterized using different chirper blocks to see the effect that each has on the output spectra. The first measurements were taken with no chirper block, and four sequential measurements were taken using a different chirper block. Each chirper block is made from a different type of glass, and has a slightly different refractive index (and dispersion). The chirper blocks measured (in order of increasing refractive index) were BK7, LF7, SF10, SF57. Measuring without a chirper block was performed at the target wavenumbers listed above, but the number of target wavenumbers was decreased in successive measurements. This was done because after measuring the spectra at the far edges of the potential bandwidth, the spectra quickly become less useful so fewer spectra needed to be taken.

2.2 Results and Discussion

The NOPA/DFG setup is clearly capable of producing MIR broadband pulses with a FWHM of at least 300 cm^{-1}. The measured results are also much lower than the potential usable bandwidth of the NOPA, which can be greater than 400 cm-1 [14]. The setup is also clearly highly tunable (can generate pulses between 1150 and 2500 cm^{-1}), and the spectra were quick to optimize. The results from two different chirper blocks (BK7 and SF10) can be seen in figure 2.2, and the rest of the results (No chirper block, LF7, SF57) can be seen in figure 2.3.

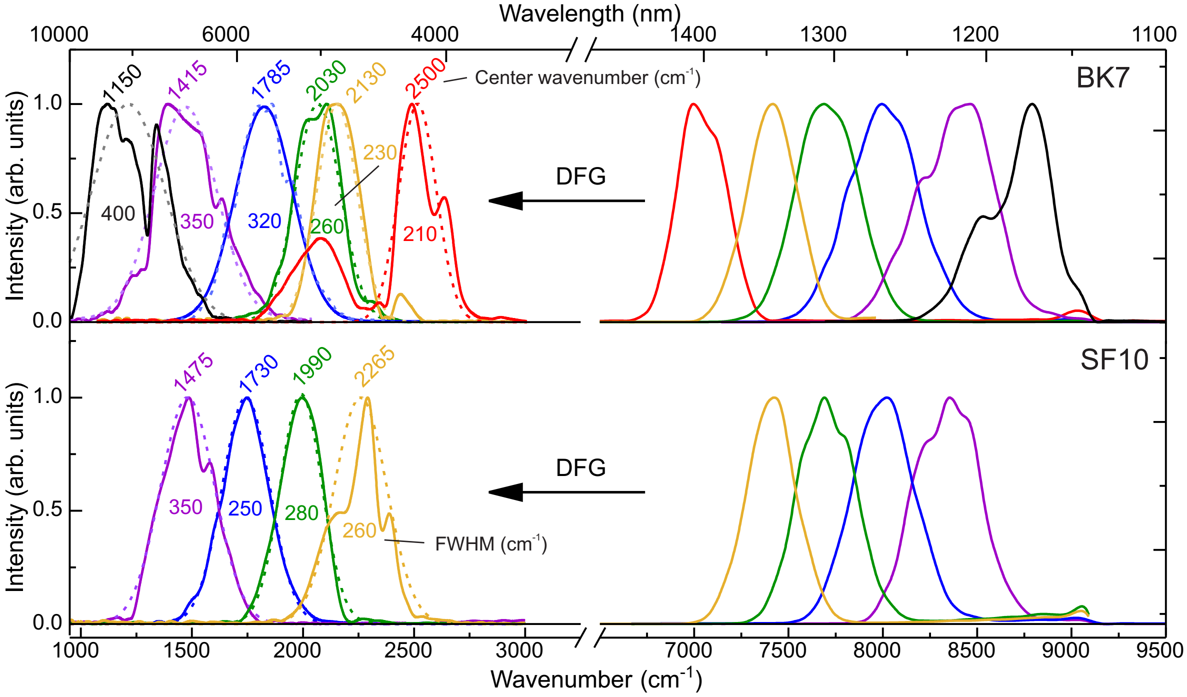

Figure 2.2: Spectra taken to characterize the NOPA/DFG using two different chirper blocks (BK7 and SF10). The spectra on the right are the NOPA spectra measured before DFG using a spectrometer. The spectra on the left are the final spectra after DFG measured using the interferometer. The target center wavenumber and the FWHM of each output spectra can be seen for each DFG spectra. To show the ideal spectra, a gaussian fit was applied to each of the DFG spectra and is represented by the dashed curves.

The results from the characterization confirmed several of the predictions about the capability of the NOPA/DFG setup. Primarily, the NOPA can produce highly broad pulses that can be converted into broad MIR pulses effectively. This is important for a variety of experiments that the setup could be used for. The pulse is sufficiently broad to be used for nanospectroscopy and spatiospectral imaging experiments (which will be discussed in the next chapter) [1,4,5]. Additionally, the broad pulses can be used for far-field spectroscopy (discussed in chapter 5) [2,8].

The characterization results also provided some interesting insight into how the chirper blocks interact and affect the output spectra. Most importantly, the addition of a chirper block dramatically increases the quality of the spectra. A chirper block reduces the number of spectral artifacts, and it also makes the spectra more gaussian. A more gaussian spectrum allows for clearer and more effective data collection, as the peaks and absorptions in the sample are easier to see. While using a reference spectrum can mitigate the problem as well, a gaussian spectrum makes the experiments easier to perform.

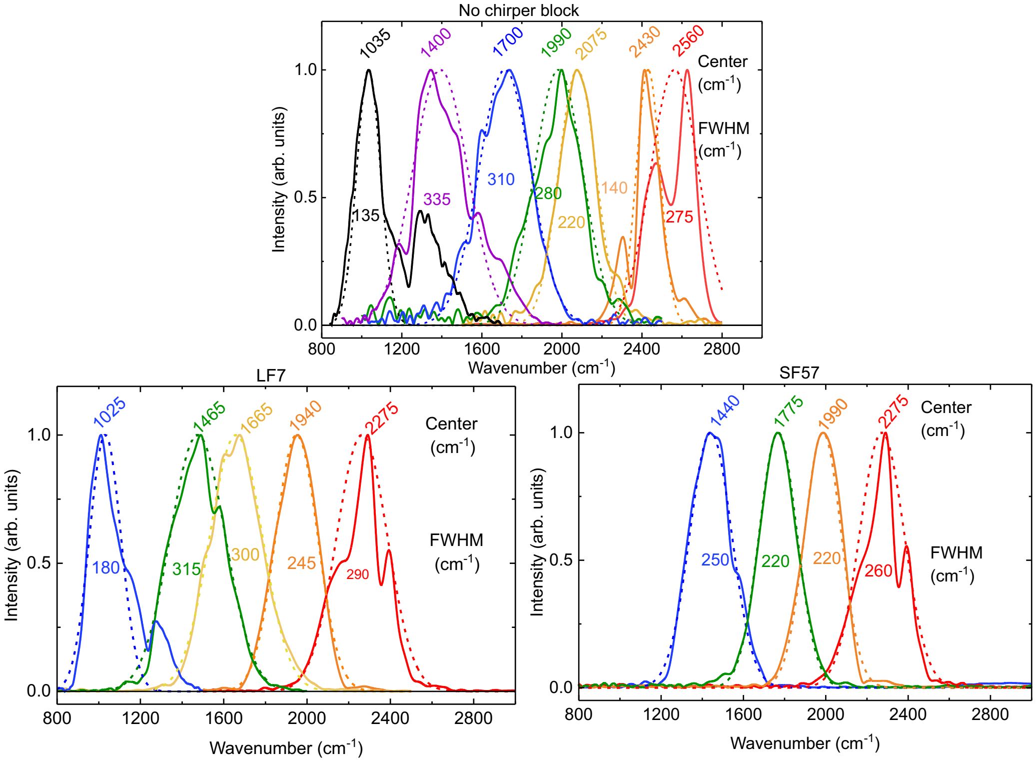

Figure 2.3: Spectra from the characterization of the NOPA/DFG setup

Compared to other light sources, NOPA/DFG performs well in the desired parameters, seen in table 2.1. Most importantly, the broad pulse from the NOPA/DFG outperforms nearly all of the other light sources in bandwidth. Additionally, the 200 fs pulse allows the NOPA/DFG to be used for experiments on the fs timescale (unlike the 60 ps pulses from a synchrotron). The NOPA pulse is also uncompressed, and the pulse duration can be shortened significantly by choosing a different laser or by adding a compressor (such as a material that is normally dispersive, i.e. Germanium) into the system [14].

Light source	Typical bandwidth	Range	Pulse duration	Repetition rate	Reference
QCL	CW	3.0-5.0μm	ns	kHz - MHz	[15]
Lead salt diodes	CW	3.3-4.2 μm	ns	kHz	[16]
OPA/DFG (Yb pumped)*	250 cm^{-1}	1.0 - 10 μm	5-200 fs	1 kHz - 10 MHz	[17]
OPO/DFG	200 cm^{-1}	2.0 - 10.0 μm	200 fs	80 MHz	[11]
OPCPA	200 cm^{-1}	2.0 - 5.0 μm	50-100 fs	1-100 kHz	[12, 13]
Supercontinuum	500 cm^{-1}	3-5.5 μm	150 fs	100 MHz	[18]
ALS (Synchrotron)	$>$3000 cm^{-1}	Unconstrained	60 ps	500 MHz	[5]
NOPA/DFG (Chen, et al.)	$>$400 cm^{-1}	5 - 11 μm	32 fs	50 kHz	[14]
NOPA/DFG (current setup)	$>$300 cm^{-1}	3.5 - 10.0 μm	200 fs	180 kHz	Experimental data

Table 2.1: MIR light source comparison table, with the measured NOPA/DFG values added.

A NOPA/DFG setup can also have significantly different parameters based on crystal choice and laser choice, and to do a complete characterization of the full possibilities of a NOPA/DFG setup would require more time. A good comparison for the potential capabilities of the NOPA/DFG setup is [14]. The paper reports a pulse duration of 32 fs at 50 kHz, showing that the NOPA pulses can be shortened significantly Additionally, the measured efficiency of the NOPA/DFG setup with a 60 mW seed and a 5 mW output is much lower at 8 % compared to the 60% measured in [14]. This is likely due to a significantly smaller pulse energy used (30 nJ in this setup compared to the 200 nJ in [14]).

One of the limiting factors of a NOPA/DFG setup is the choice of crystal. For BBO and LGS (NOPA OPA and DFG respectively), a higher repetition rate ($>$ 1 MHz) has the potential to damage the crystal. A lower repetition rate can cause issues when measuring molecular signals, and the challenges that this raises will be discussed in the next chapter.

Chapter 3

IR s-SNOM on PTCDA

3.1 Introduction

Once the characterization was complete, a proof of principle experiment was done using the NOPA/DFG setup to perform IR s-SNOM on Perylenetetracarboxylic dianhydride (PTCDA). The intention of the experiment was to show if the NOPA/DFG setup provided any significant advantages or disadvantages over other traditional light sources.

PTCDA is an organic semi-conductor that forms microcrystals. The absorption of the microcrystals is highly dependent on crystal orientation, which can be upright or flat. The upright orientation exhibits a strong molecular response at 1780 cm^{-1}, while the flat form does not. The difference in absorption is due position of the carbonyl relative to the AFM tip. The near-field signal is polarized so that the signal is perpendicular to the surface of the sample, if the scattered signal from the tip is parallel to the carbonyl (upright), the signal will be much stronger than if it is perpendicular (flat). The comparison between the orientations can be seen in figure 3.1. IR s-SNOM can be performed to measure the response of the microcrystal, allowing it to be identified. PTCDA was chosen due to its strong absorption, as well as its high availability and low cost. The material has also been measured previously [1, 5], which would provide an excellent comparison for the NOPA/DFG setup.

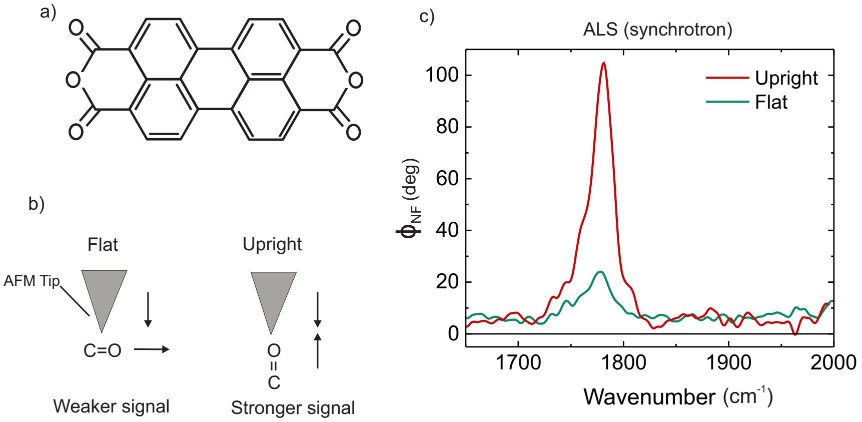

Figure 3.1: **(a)** Structure of Perelenetetracarboxylic dianhydride (PTCDA). **b)** Representation of the difference in signal due to the orientation of the crystal. If the carbonyl is perpendicular (flat) to the AFM tip, then the signal will be weaker, but if it is parallel (upright) to the AFM tip, then the signal will be much stronger. **c)** Spectra of two PTCDA microcrystals showing the difference in response at 1780 cm^{-1}. The upright orientation has a much larger response than the flat orientation, and the microcrystal can be identified by the absorption strength (data from Ref [1]).

Performing IR s-SNOM on PTCDA using a NOPA/DFG setup provided a method to prove that the setup is a viable option for broadband MIR pulse generation.

3.2 Methods

Sample Preparation

The samples were prepared by evaporation of PTCDA on an Au substrate by postdoctoral fellow Roland Wilcken. After evaporation the samples were placed under an optical microscope to determine if crystals were present. For the higher concentration solution, the crystals were far too large ($> 1\mu$m) to be used with the Innova AFM, so the smaller concentration sample was chosen for measurement.

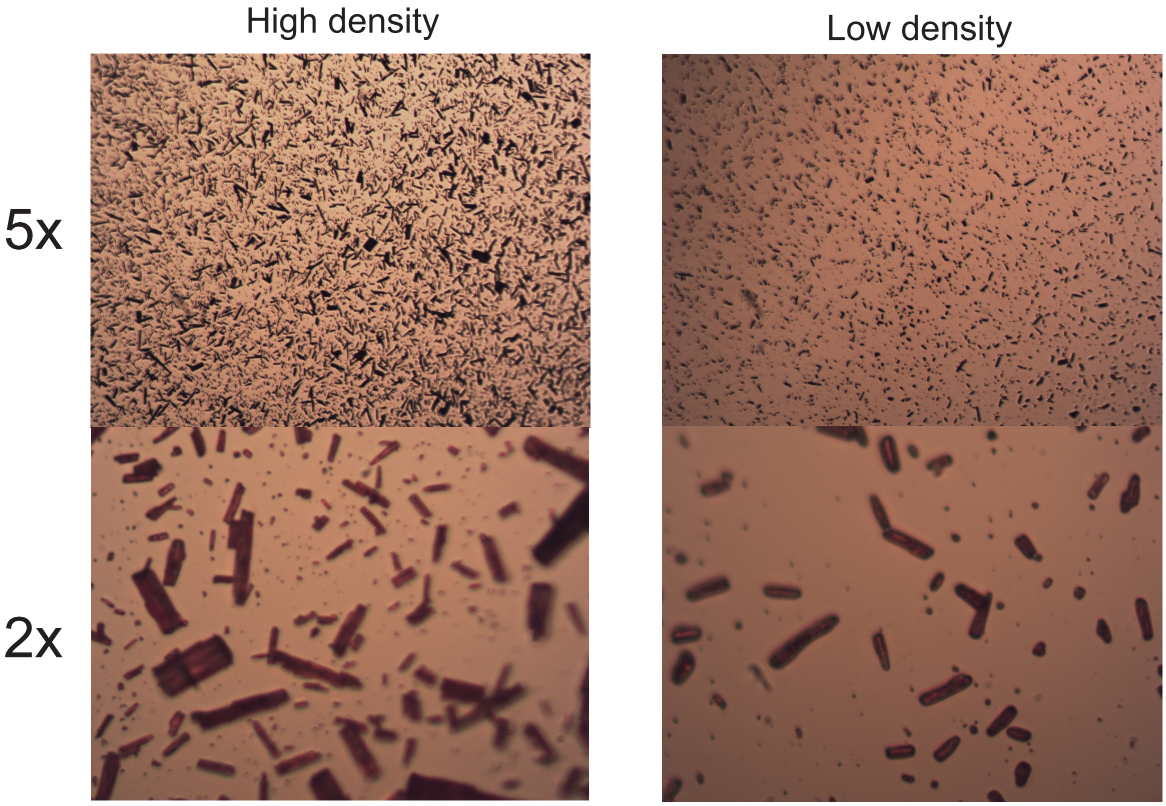

Figure 3.2: Images of the high density and low density samples taken with an optical microscope. The high density sample created crystals that were too large to be used. The lower density sample provided much more reasonably sized crystals that could be measured effectively. The larger crystals were still too large to be measured, but the smaller microcrystals (small dark spots) were sized correctly.

IR s-SNOM on PTCDA

Once the samples were prepared, the setup was tuned for measurement. As in the characterization experiment, a spectrometer (APE waveScan) was placed in the beam directly after the NOPA, and the NOPA spectrum was tuned to the target wavelength (1249 nm) to measure the upright orientation absorption peak at 1780 cm^{-1}. Once the target wavelength was reached, the signal was optimized so that the bandwidth was maximized while ensuring high power. After it was determined that the NOPA spectrum was sufficient, the DFG was optimized in a similar fashion, using a power meter instead of a spectrometer.

The generated MIR pulse needed to be co-aligned with a HeNe laser so that the MIR beam could be aligned onto the AFM tip. After co-alignment, the AFM camera was centered onto the tip so that the targeted crystal could be seen. Then, A washer was placed in the AFM to begin the alignment process. The washer provided a rough surface that made the HeNe easy to see as it scattered on the sample. The HeNe was aligned to the camera crosshairs, and then the washer was removed.

An Au reference sample was used for its high reflectivity and lack of absorption in the range to ensure that the beam was focused onto the tip and interference could be seen. The reference was placed in the AFM and a suitably clean portion was chosen. The tip was engaged and the tip approached the sample. Once the tip was fully engaged, if the HeNe and MIR pulses had been aligned properly, the near-field signal would be detected. Due to the high reflectivity of gold, the signal was large ($> 100\ \mu$V) and easy to see. An interferogram was then measured to determine the laser spectrum on the sample.

If the spectrum was sufficient to see the response on PTCDA, the tip was disengaged and the setup was allowed to purge to remove as much water in the air as possible. Once the humidity inside the setup was approximately $3 - 4\%$, the tip was re-engaged and the final reference spectrum was taken. This spectrum would be necessary later to remove any defects from the laser spectrum.

The PTCDA sample was now placed into the AFM and the position was adjusted so that a region with several potential crystals could be targeted. The Innova AFM has a relatively small scan range $< 50\ \mu$m in each direction, so positioning the sample in this way was important. As many of the crystals were still too large to be measured, a region with a few small crystals was ideal. Once a region was found, the tip was engaged and the signal was found again. With the tip engaged, an AFM scan across the region was taken to find a specific crystal to measure. When a potential candidate was found (approximate crystal size $< 2\ \mu$m, but > 100 nm), the AFM tip was moved to a position on the microcrystal so that the localized near-field response could be measured. Using the tip in this way allows for the signal to be highly localized, and is one of the primary advantages of this particular method. An image showing the region that contained the upright crystal measured, as well as the AFM topography and tapping phase images can be seen in figure 3.3

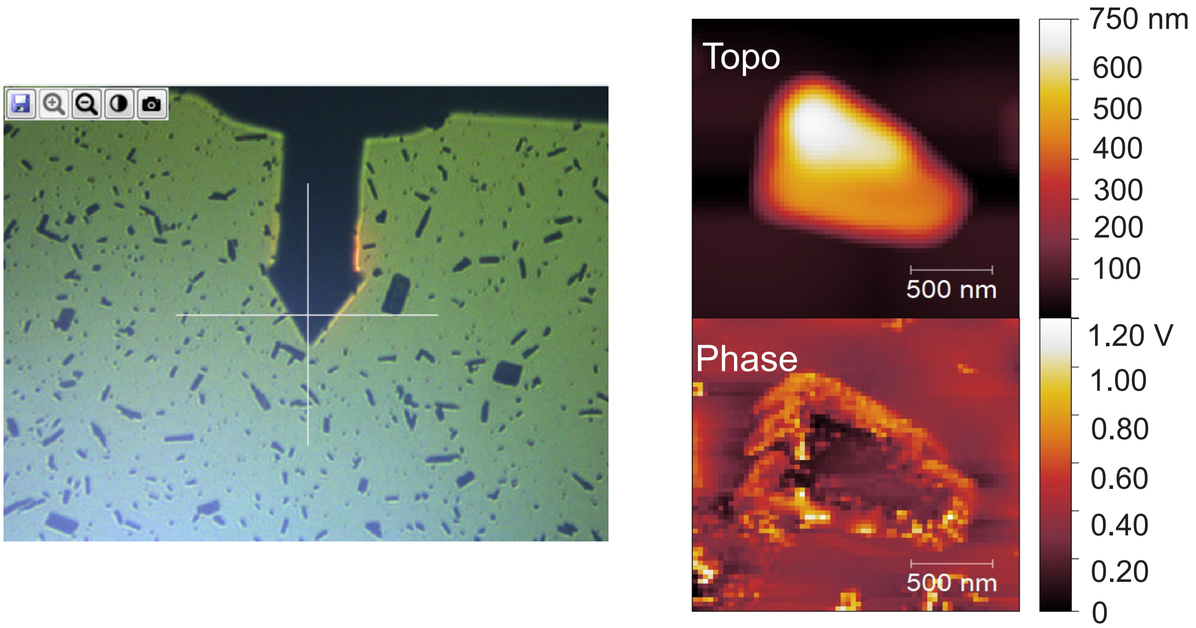

Figure 3.3: **Left)** AFM camera image taken of the position of the upright crystal measured. **Right)** the generated AFM images of the topography (topo) and tapping phase (phase) of the upright crystal.

As before, an interferogram was then taken by adjusting the optical path length difference in the reference arm, and the variation in the time domain was convered into the frequency domain by Fourier transform. The spectrum on that specific microcrystal could then be seen, and it could be determined if the microcrystal has an upright or flat orientation. The goal of the experiment was to find crystals in both formations, and it was performed on several crystals to see any potential differences.

3.3 Results and Discussion

The results from the IR s-SNOM experiment on PTCDA can be seen in figure 1.2. There is a clear difference between the upright and flat orientations of two different crystals, and this can be seen in the near-field phase response of the material.

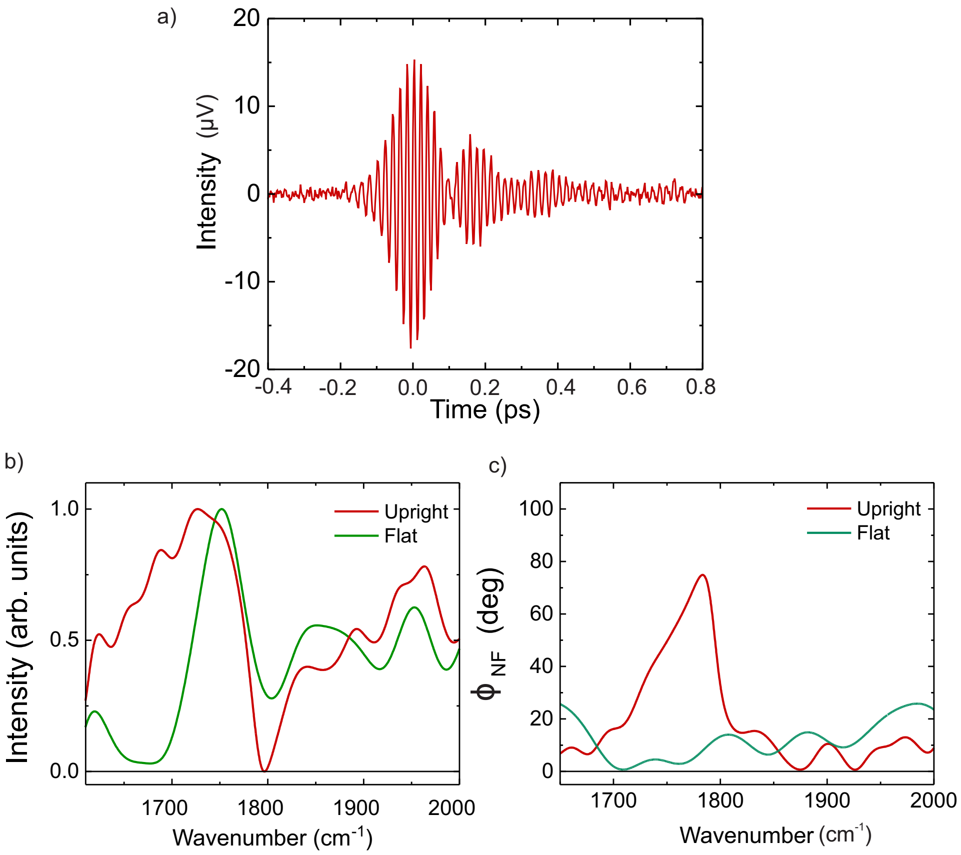

Figure 3.4: PTCDA IR s-SNOM experiment results. **a)** Generated interferogram from one reference arm scan. The interferograms of 20 scans were averaged together, and the results were converted into the frequency domain by fourier transform. **b)** Amplitude component of the near-field signal. **c)** Phase component of the near-field signal. This can be interpreted as the absorption spectra of the material. The peak at 1749 cm^{-1} can be seen in the upright microcrystal orientation, but not the flat orientation.

From these results, it can be seen that a NOPA/DFG setup can be used for IR s-SNOM. However, to determine the full effectiveness of the experiment, the NOPA/DFG data should be compared with another light source. A comparison set of data can be seen with the NOPA/DFG phase response in figure 3.5.

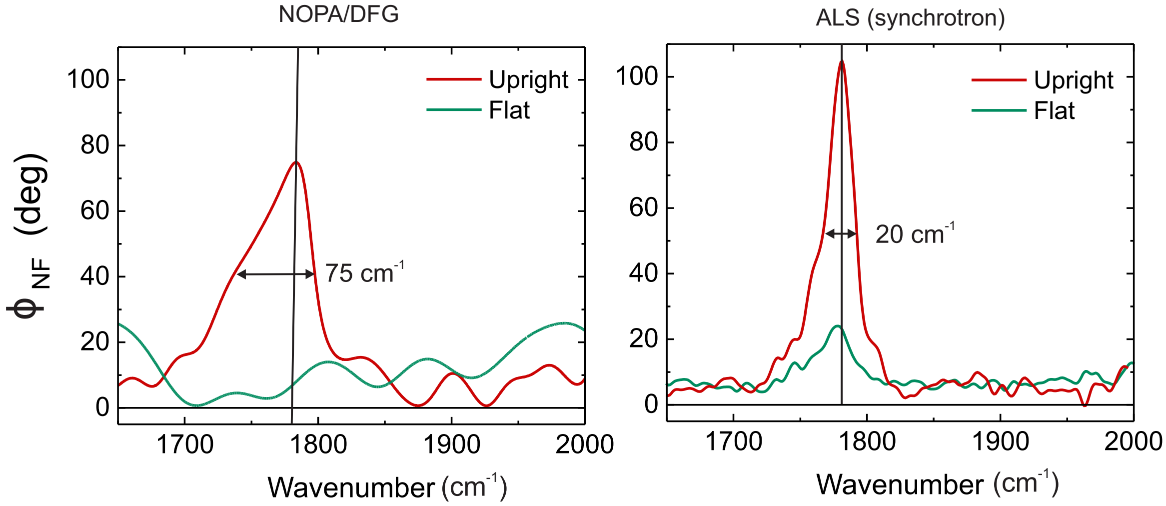

Figure 3.5: Results from the NOPA/DFG IR s-SNOM experiment on PTCDA compared to the results from the same experiment performed using a synchrotron (synchrotron data from Ref [1]).

The NOPA/DFG results are similar to the ALS results, but there are a few differences. The most significant difference is the resolution between the two data sets. The ALS appears to have a much higher spectral resolution than the NOPA/DFG for this data set. This result is unexpected, and there are a few potential explanations. The primary explanation is that the signal to noise ratio of the NOPA/DFG is too low, meaning that more scans needed to be taken so that averaging could remove as much noise as possible. The high number of scans also indirectly caused the scanning range to be shortened. In order to have a higher spectral resolution, a longer range scan should be taken. This creates a problem when combined with a higher number of scans. If the measurement takes too long, the data takes too long, the results can be affected. For longer measurements, the AFM tip can drift off of its position on the sample. Additionally, a long measurement can potentially damage the sample due to the high amount of power being sent onto the surface of the sample. Given more time it would make sense to try this experiment again and see if the resolution remains poor with a longer scan range.

While these results are preliminary, they do demonstrate that this type of experiment may not be ideal for the NOPA/DFG. For resolving a single peak with a linewidth of a few wavenumber, there are other light sources that are easier and more effective (OPA/DFG, OPO, OPCPA). There are other experiments where a NOPA/DFG setup can prove invaluable however. For example, measurements on nanostructures that have much higher enhancement (which improves the signal to noise) require a spectrum that is much broader > 300 cm^{-1} than a traditional OPA/DFG can provide (see [3]). Additionally, the next section will discuss another experiment where a NOPA/DFG setup is a very effective light source.

Chapter 4

Fabry-Perot Cavities

4.1 Introduction

Another potential use of the NOPA-DFG setup is for far-field spectroscopy. One application of this is for studying Vibrational Strong Coupling (VSC). Similar to classical pendula, molecules can form coupled systems with photons if frequency of the light is close enough to the resonance frequency of the molecular excitation [2]. The molecules and photons are said to strongly coupled if the energy exchange between the molecule and the electromagnetic field is faster than the rate of energy dissipation. The coupled system can no longer be described as a molecule and a photon, and instead form a hybrid state known as a Vibro-Polaritonic (VP) mode (in the case of VSC), and studying these modes can provide valuable insight into chemical and molecular interactions. If a VP mode is formed, it can be seen as splitting in the spectrum of the system. However, a splitting in the spectrum does not necessarily confirm the presence of strong coupling. Instead, the coupled modes can only be confirmed by observing an "anti-crossing" in the dispersion curve of the system. An example of a dispersion curve demonstrating anti-crossing can be seen in figure 4.1. The details of VSC are beyond the scope of this paper, but for a more rigorous discussion see: [2, 8].

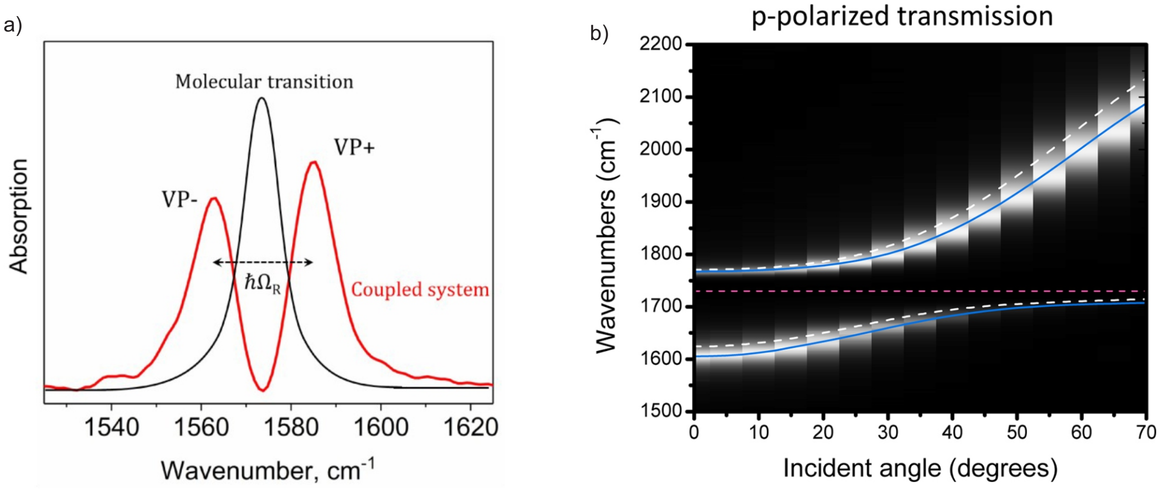

Figure 4.1: **a)** Absorption spectra showing the VP modes of a system that is strongly coupled. The Rabi splitting $\hbar\Omega_R$ can be used to determine the coupling strength of the system. From Ref [2]. **b)** Dispersion curve of a PMMA Fabry-Perot (FP) cavity. The anti-crossing of the two branches can be seen, indicating coupling between the photon and molecule. The coupling strength can be determined by the minimum splitting between the two branches. From Ref [8]

Vibrational Strong Coupling can be difficult to achieve, but one of the most straightforward experiments to see VSC is through the use of Fabry-Perot (FP) cavities. An FP cavity is an optical cavity between two parallel highly reflective mirrors [2]. The cavity has a resonance frequency which is determined by the thickness of the cavity. If the resonance frequency of the cavity matches the resonance frequency of the molecules, then the molecules will couple to the cavity. The addition of photons to the system increases the coupling strength, but in an FP cavity, the coupling modes are created even in the absence of external light. An FP cavity can be created in both the liquid and solid phase, and both phases were explored.

The NOPA-DFG setup is valuable for these experiments because it can provide a broadband pulse in the desired region (MIR for Vibrational Strong Coupling). For this paper, the setup was used to characterize Poly(methyl methacrylate) (PMMA) Fabry-Perot cavities, as well as to characterize an air filled liquid cell.

4.2 Methods

Sample Preparation

Before the samples could be made, it was important to determine a method to make PMMA films of consistent thickness. This was done by spin coating different solutions of PMMA onto $\mathrm{CaF_2}$ windows and measuring the absorbance of the film using FTIR. The precise thickness was difficult to determine, but an approximate thickness could be determined by measuring a known thickness of PMMA and comparing it to the sample films. The known solution was a 0.053M (c) solution of PMMA that was placed in a liquid cell with a thickness (d) of 100 μm. Using the measured absorbance (OD), the value of ϵ could be determined using the following equation:

$$\epsilon = \frac{\mathrm{OD}}{\mathrm{c} \cdot \mathrm{d}} \tag{4.1}$$

The thickness of the unknown film could be determined using the density of PMMA ($\rho = 1.18$ gm/cm^3), and the solid state concentration, $\mathrm{c}_s = \rho/M$. Solving for thickness in equation 5.1 gives:

$$\mathrm{d} = \frac{\mathrm{OD}}{\epsilon \cdot \mathrm{c}_s} \tag{4.2}$$

For this experiment the calculated value $\epsilon = 398.095$ L/mol·cm. As an example calculation: For a solid state concentration of 0.012 mol/cm^3, and a measured film OD of 0.42, the film thickness can be calculated as follows:

$$\mathrm{d} = \frac{0.42}{3.98095\ [\mathrm{L/(mol \cdot cm)}] \cdot 0.012\ [\mathrm{mol/cm^3}]} = 894.088\ [\mathrm{nm}] \tag{4.3}$$

Using this equation, the thickness could be calculated, although this calculation was approximate due to the uneven film thickness of the solid state cavities. The film thickness was determined for different spin coating speeds (750, 1000, 1250 rpm) and concentrations (1.25, 1.5, 1.75M), and the results can be seen in figure 4.2

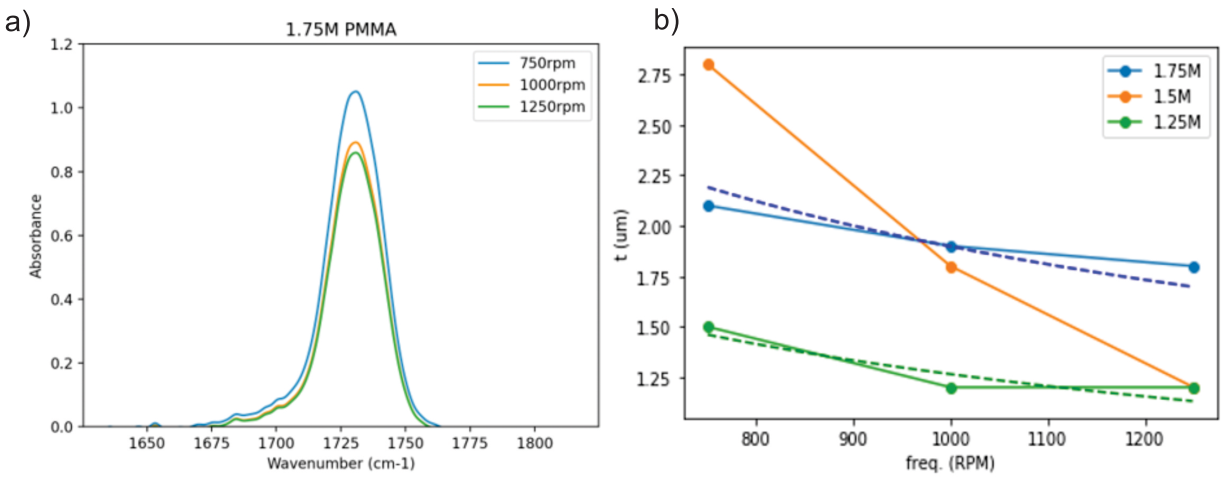

Figure 4.2: **a)** Absorbance data of PMMA films with different spin coating speeds using a 1.75M PMMA solution. The absorbance of the sample was measured using FTIR. **b)** Plot comparing the PMMA film thickness from different spin casting speeds and solution concentrations. The ideal film thickness is 2 μm, which can be achieved through a few different combinations of spin speeds and concentrations (plot made by graduate student Richard Puro).

Once a film thickness could be consistently recreated, the FP cavities could be made. For all the samples, a CaF_2 substrate was coated with a thin layer 10 nm of SiO_2 for protection, and then coated with Au using an evaporator. The Au films were between 10 and 20 nm, and would act as one of the parallel mirrors in the FP cavity. Then the cavities were coated with PMMA primarily using spin coating (drop casting was also attempted, but rather unsuccessful). PMMA was chosen because it is highly available, has a strong resonance at 1749 cm^{-1}, and it forms films easily. To coat the samples in PMMA, the PMMA was dissolved in acetonitrile to create a 1.75M solution, and a few drops were placed onto the Au coated CaF_2 windows. Then the sample was spun at 1000 rpm to remove any excess acetonitrile. After spinning, a film of PMMA would be left on the surface of the sample. After the spin coating, another layer of Au was evaporated onto the samples to provide the second mirror. The results from the film thickness calculations can be seen in The cavity layout and a photo of one of the cavities can be seen in figure 4.3.

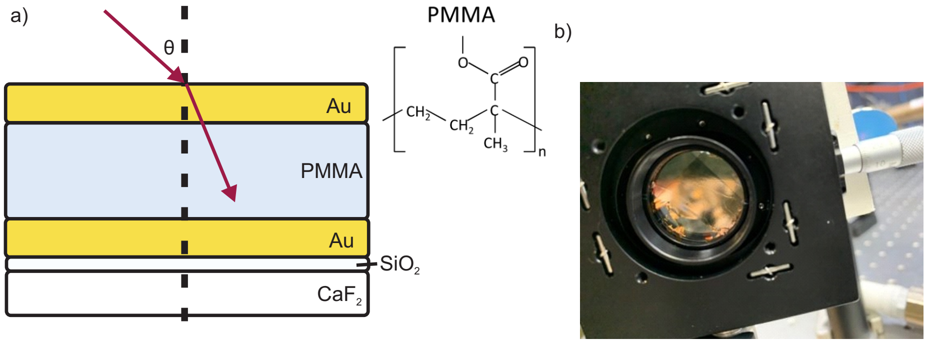

Figure 4.3: **a)** Schematic of a PMMA Fabry-Perot cavity. The samples were measured in transmission, and the incident angle θ was increased to perform a full characterization of the cavity resonance. **b)** A photo of one of the cavities made placed in a sample holder to be characterized. The uneven film thickness can be seen, but the sample was tested to determine the importance of the even thickness, and to see if strong coupling could be seen regardless.

Cavity Characterization

To determine the quality of the cavity (and to see if VSC could be achieved), the sample was placed into the far-field path of the setup (see figure 1.3. The spectrum was measured in the same manner as for the NOPA characterization (without use of the AFM), and the transmission of the cavity was recorded. To get a full description of the cavity, the spectrum must be measured at difference incident angles between the sample and the laser. By sweeping through the angles, both peaks will shift toward higher wavenumbers, with the lower peak shifting until it reaches the resonance of the coupled molecule (PMMA in this case). The spectrum at each angle (0, 10, 15, 20, 30, and 40 degrees) was recorded and then were each plotted on the same plot to see any clear trends in the peaks.

Liquid phase Fabry-Perot cavities

Fabry-Perot cavities can also be created in the liquid phase. Strong coupling in the liquid phase is easier to accomplish because of cooperative coupling [2]. In cooperative coupling, both the solute and solvent molecules can couple, increasing the number of oscillators and dramatically increasing the signal strength. As another potential experiment, a liquid cell was designed and machined to hold molecules in solution to be measured in the far-field in the same way as the solid state FP cavities. A schematic of the liquid cell and some images of the machined cell can be seen in figure 4.4.

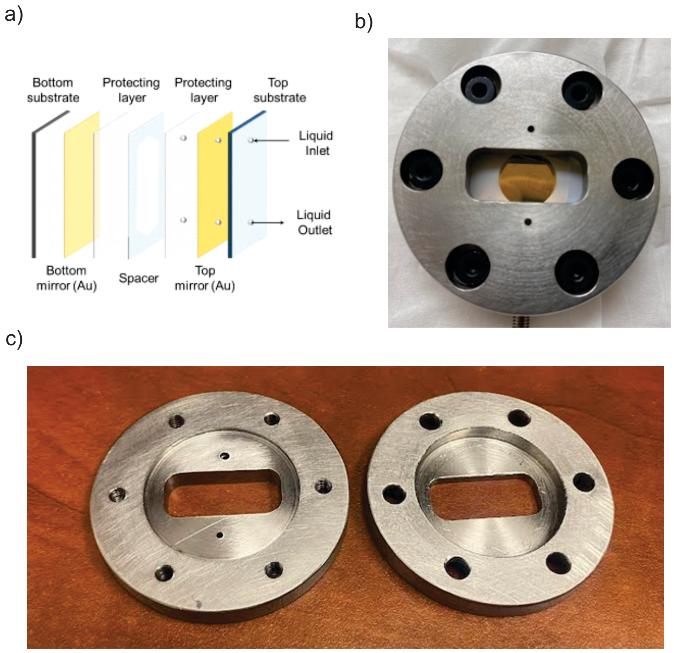

Figure 4.4: **a)** Schematic of a liquid cell FP cavity. The substrate chosen is CaF_2. The inlet and outlet holes allow for molecule in solution to be placed inside the cell, and the spacer determines the thickness of the solution. Figure from Ref [2]. **b** Photo showing the liquid cell fully assembled with Au coated CaF_2 windows in place. A interference pattern can be seen on the surface of the Au. By looking at the interference pattern and adjusting the outer screws, the cavity can be tuned to achieve the proper thickness. **c)** Photo of the two main pieces of the machined liquid cell separated so the general design can be seen. The windows are placed in a cut region in the center of the cell, and the two halves are screwed together. The small inlet and outlet holes can be seen in the piece on the left.

4.3 Results and Discussion

Solid-state FP cavities

The results from the PMMA solid state cavities can be seen in figure 4.5. A splitting can be seen between the two peaks at the PMMA carbonyl absorption at 1749 cm^{-1}. The splitting is approximately 120 cm^{-1}, which is much greater than the linewidth of the PMMA absorption of 20 cm^{-1}. This means that the cavity is in the strong coupling regime, but to determine if strong coupling occurs, anti crossing must be seen in the dispersion curve.

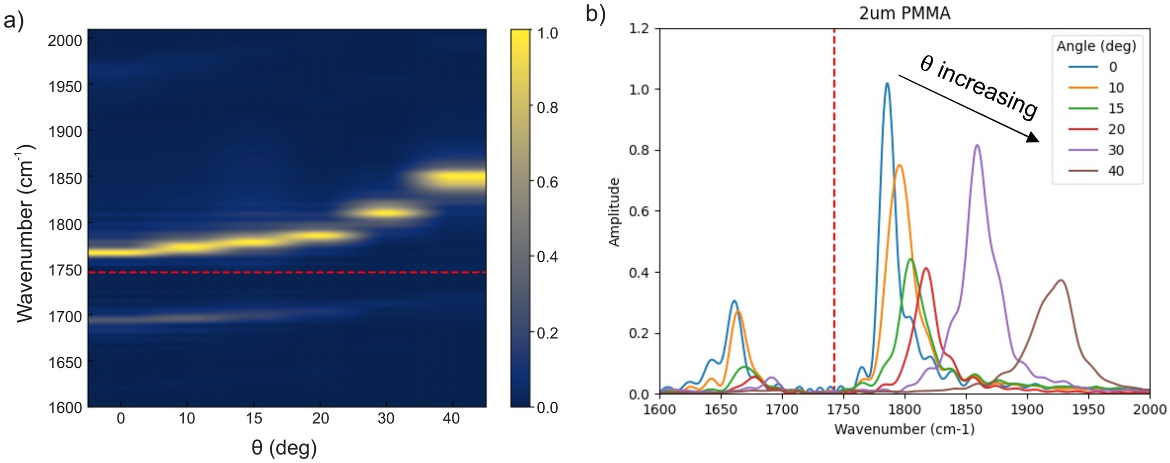

Figure 4.5: Results from the solid state PMMA FP cavity. **a)** Dispersion curve showing the peak splitting as a function of incident angle. Anti-crossing can be seen around 20 degrees. **b)** Measured spectra of the characterization plotted as a function of wavenumber. These plots are the same data, just visualized in different ways. The splitting between the peaks is 120 cm^{-1}, which means that the sample is in the strong coupling regime. Since the dispersion curve also shows anti-crossing, then it can be determined that the molecules and the photons are strongly coupled.

Liquid-state FP cavities

Due to the brittleness of CaF_2, the window that was drilled to allow liquid solution to be placed into the cell was cracked, and the liquid was unable to be used until new windows arrived. Instead, the cell was characterized using air to observe the free spectral range (FSR) and linewidth of the peaks. The results can be seen in figure 4.6. The characterization of the cavity is ongoing.

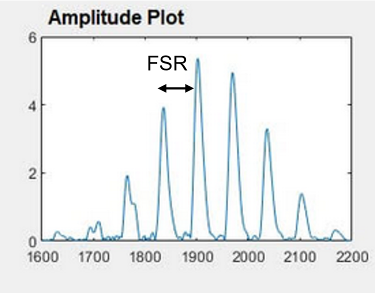

Figure 4.6: Plot showing the characterization of the liquid cell using air. The free spectral range can be used with the FWHM of the cavity mode to determine the quality factor Q of the cavity. A higher Q corresponds with stronger coupling

NOPA results

While these results are interesting, they are intended to showcase one of the main advantages of the NOPA/DFG, which is the large bandwidth. Both of these experiments were able to be performed with a single tuning of the NOPA. The broad bandwidth allows the full extent of the cavity resonance to be observed, as well as the entirety of the splitting between the peaks. As the coupling strength increases, the splitting will increase as well, which can be a challenge to measure with some traditional MIR light sources. This is not an issue for far-field measurements, but could become an issue for near-field measurements. A logical next step for this experiment is to create FP cavities small enough to fit into the Innova AFM, which can then be measured in the near-field. This type of experiment has not been explored and could provide interesting results.

Conclusions and Outlook

The NOPA/DFG has many potential uses as a broadband light source. The experiments performed show that the bandwidth provided by the NOPA/DFG setup can be invaluable for some experiments. The ultrafast pulse also allows for exploration of molecular vibrations and interactions on the fs timescale, which is something that cannot be done with other highly broad light sources. Additionally, the high tunability of the NOPA allows for many different experiments to be performed quickly and effectively. These advantages are essential for many of the experiments that a NOPA/DFG might be used for, and the setup is a unique addition to the potential light sources for these experiments.

There is much more work to be done exploring and characterizing the pulses generated from a NOPA/DFG. In particular, plasmonic enhancement and light-matter coupling experiments provide many potentially fascinating experiments that have yet to be performed. Many of the traditional light sources used for these experiments are only effective for far-field measurements, and near-field measurements could provide more localized information about these structures and interactions. For light-matter coupling experiments, there is a distinct lack of near-field experiments in the field, and there are some preliminary results on the cavities made in this paper that need to be explored further.

Acknowledgements

I would like to thank all the members of the CU Nano-optics group for all their help on this project and this paper. In particular I would like to thank postdoctoral fellow Roland Wilcken, graduate student Richard Puro, undergraduate research assistant Dylan Wharton, and principal investigator Markus Raschke for the extensive amount of time and effort they spent working with me. This paper would not have been possible without them teaching me how to perform the experiments, helping me to understand the high level physics and chemistry necessary, and providing me with the literature resources to facilitate my own learning as well.

Bibliography

[1] Eric A. Muller, Benjamin Pollard, Hans A. Betchel, Peter van Blerkom, and Markus B. Raschke. Infrared vibrational nanocrystallography and nanoimaging. *Science Advances*, 2, 2016.

[2] Kalaivanan Nagarajan, Anoop Thomas, and Thomas Ebbesen. Chemistry under vibrational strong coupling. *Journal of the American Chemical Society*, 143, 2021.

[3] Christian Huck, Jochen Vogt, Michael Sendner, Daniel Hengstler, Frank Neubrech, and Annemarie Pucci. Plasmonic enhancement of infrared vibrational signals: Nanoslits versus nanorods. *ACS Photonics*, 2:1489–1497, 2015.

[4] Eric A. Muller, Benjamin Pollard, and Markus B. Raschke. Infrared chemical nano-imaging: Accessing structure, coupling, and dynamics on molecular length scales. *The Journal of Physical Chemistry Letters*, 6, 2015.

[5] Hans A. Bechtel, Samuel C. Johnson, Omar Khatib, Eric A. Muller, and Markus B. Raschke. Synchrotron infrared nano-spectroscopy and -imaging. *Surface Science Reports*, 75, 2020.

[6] Thomas P. Gray. Infrared nano-imaging and spectrosocpy of quantum vibrational coupling in molecular systems. 2022.

[7] Xinzhong Chen, Debo Hu, Ryan Mescall, Guanjun You, D.N. Basov, Qing Dai, and Liu Mengkun. Modern scattering-type scanning near-field optical microscopy for advanced materials research. *Advanced Materials*, 31, 2019.

[8] J.P. Long and B.S. Simpkins. Coherent coupling between a molecular vibration and fabry-perot optical cavity to give hybridized states in the strong coupling limit. *ACS Photonics*, 2:130–136, 2015.

[9] Krzysztof B. Bec, Justyna Grabska, and Christian W. Huck. Biomolecular and bioanalytical applications of infrared spectroscopy - a review. *Analytica Chimica Acta*, 1133:150–177, 2020.

[10] Margherita Maiuri, Marco Garavelli, and Giulio Cerullo. Ultrafast spectroscopy: State of the art and open challenges. *J. Am. Chem. Soc.*, 142:3–15, 2020.

[11] Suddapalli Kumar Chaitanya, Adolfo Esteban-Martin, Takuro Ideguchi, Ming Yan, Simon Holzner, Theodor W. Hansch, Nathalie Picque, and Majid Ebrahim-Zadeh. Few-cycle, broadband, mid-infrared optical parametric oscillator pumped by a 20-fs ti:sapphire laser. *Laser and Photonics Reviews*, 8, 2014.

[12] M.R. Gerrity, S. Brown, T. Popmintchev, M.M. Murnane, H.C. Kapteyn, and S. Backus. High repetition rate, mj-level, mid-ir opcpa system. CLEO:2014. Optica Publishing Group, 2014.

[13] B.W. Mayer, C.R. Phillips, L. Gallmann, and Keller. U. Mid-infrared pulse generation via achromatic quasi-phase-matched opcpa. *Optics Express*, 22, 2014.

[14] Bo-Han Chen, Emmanuel Wittmann, Yuya Morimoto, Peter Baum, and Eberhard Riedle. Octave-spanning single-cycle middle-infrared generation through optical parametric amplification in **LiGaS**. *Optics Express*, 27, 2019.

[15] Ralf Ostendorf et al. Recent advances and applications of external cavity-qcls towards hyperspectral imaging for standoff detection and real-time spectroscopic sensing of chemicals. *Photonics*, 3:28, 2016.

[16] A. Khiar, V. Volobuev, M. Witzan, A. Hochreiner, M. Eibelhuber, and G. Springholz. In-well pumped mid-infrared pbte/cdte quantum well vertical external cavity surface emitting lasers. *Applied Physics Letters*, 104:231105, 2014.

[17] C. Manzoni and G. Cerullo. Design criteria for ultrafast optical parametric amplifiers. *Journal of Optics*, 18, 2016.

[18] Alexander J. Lind, Abijith Kowligy, Henry Timmers, Flavio C. Cruz, Nima Nader, Myles C. Silfies, Thomas K. Allison, and Scott A. Diddams. Mid-infrared frequency comb generation and spectroscopy with few-cycle pulses and $\chi^{(2)}$ nonlinear optics. *Physical Review Letters*, 124, 2020.

[19] S. Maghsoudy-Louyeh, M. Kropf, and B.R. Tittmann. Review of progress in atomic force microscopy. *The Open Neuroimaging Journal*, 12, 2018.

[20] Hang Zhang, Junxiang Huang, Yongwei Wang, Rui Liu, Xiulan Huai, Jingjing Jiang, and Chantelle Anfuso. Atomic force microscopy for two-dimensional materials: A tutorial review. *Optics Communications*, 406, 2018.

[21] Jun Nishida, Peter T. S. Chang, Jiselle Y. Ye, Prachi Sharma, Dylan M. Wharton, Samuel C. Johnson, Sean E. Shaheen, and Markus B. Raschke. Nanoscale heterogeneity of ultrafast many-body carrier dynamics in triple cation perovskites. *Nature Communications*, 13, 2022.

[22] Peter Q. Liu, Anthony J. Hoffman, Matthew D. Escarra, Kale J. Franz, and Jacob B. Khurgin. Highly power-efficient quantum cascade lasers. *Nature Photonics*, 4, 2010.

[23] Gustavo Villares, Andreas Hugi, Stephane Blaser, and Jerome Faist. Dual-comb spectroscopy based on quantum-cascade-laser frequency combs. *Nature Communications*, 5, 2014.

[24] Christine Y. Wang, Lyuba Kuznetsova, V.M. Gkortsas, L. Diehl, and F.X. Kartner. Mode-locked pulses from mid-infrared quantum cascade lasers. *Optics Express*, 17, 2009.

[25] C. L. Felix, W.W. Bewley, I. Vurgaftman, J.R. Lindle, and J.R. Meyer. Low-threshold optically pumped $\lambda = 4.4\mu$m vertical-cavity surface-emitting laser with a **PbSe** quantum-well active region. *Applied Physics Letters*, 78:3770–3772, 2001.

[26] J. Limpert, F. Roser, T. Schreiber, and A. Tunnerman. High-power ultrafast fiber laser systems. *IEEE Journal of Selected Topics in Quantum Electronics*, 12:233–244, 2006.

[27] Julie A. Gruetzmacher and Norbert F. Scherer. Few-cycle mid-infrared pulse generation, characterization, and coherent propagation in optically dense media. *Review of Scientific Instruments*, 73, 2002.

[28] C.J. Fecko, J.J Loparo, and A. Tokmakoff. Generation of 45 femtosecond pulses at 3μm with a **KNbO**$_3$ optical parametric amplifier. *Optics Communications*, 241:521–528, 2004.

[29] Tyler W. Neely, Todd A. Johnson, and Scott A. Diddams. High-power broadband laser source tunable from 3.0μm to 4.4 μm based on a femtosecond yb:fiber oscillator. *Optics Letters*, 36, 2011.

[30] Darren D. Hudson, Matthias Baudisch, Daniel Werdehausen, Benjamin J. Eggleton, and Jens Biegert. 1.9 octave supercontinuum generation in a **As**$_2$**S**$_3$ step-index fiber driven by mid-ir opcpa. *Optics Letters*, 39, 2014.

[31] C. Homann, C. Schriever, P. Baum, and E. Riedle. Octave wide tunable uv-pumped nopa: pulses down to 20 fs at 0.5mhz repetition rate. *Optics Express*, 16, 2008.

[32] M. Liebel, C. Schnedermann, and P. Kukura. Sub-10-fs pulses tunable from 480 to 980 nm from a nopa pumped by an **Yb:KGW** source. *Optics Letters*, 39, 2014.

[33] Q.Z Wang, P.P. Ho, and R. R. Alfano. *The Supercontinuum Laser Source: Fundamentals with Updated References*. Springer, 2006.

[34] Emanuel Wittmann. Taming optical parametric amplification. 2019.

[35] Govind P. Agrawal. *Nonlinear Fiber Optics (Sixth Edition)*. Academic Press, 2006.

[36] Robert W. Boyd. *Nonlinear optics (3rd Edition)*. Academic Press, 2008.